Visualization Analysis of Covalent and Noncovalent Interactions in Real Space

Tian Lu

Beijing Kein Research Center for Natural Sciences, Beijing 100024, P. R. China

Author information

Tian Lu ORCiD: 0000-0002-1822-1229 E-mail: sobereva@sina.com

Abstract: Understanding the types and locations of interactions between atoms or molecules within a chemical system is a fundamental concern in chemistry. In the field of theoretical and computational chemistry, wavefunction analysis offers various methods based on functions defined in three-dimensional real space, enabling the visual representation of both covalent and noncovalent interactions. These methods provide researchers with an intuitive understanding of molecular interactions and are gaining increasing attention. This review systematically introduces various widely adopted and distinctive visualization methods, such as the noncovalent interaction (NCI) method, the independent gradient model based on Hirshfeld partition of molecular density (IGMH), the interaction region indicator (IRI), the electrostatic potential (ESP), the electron localization function (ELF), and deformation density. Additionally, numerous application examples are provided to help readers recognize the significant practical value of these methods. Also the computer program Multiwfn, which effectively implemented all the introduced methods, is briefly mentioned.

Keywords: chemical bond; weak interaction; covalent interaction; noncovalent interaction; wavefunction analysis

1. Introduction

Interactions in chemical systems can be divided into two main categories: chemical bonds and weak interactions. Chemical bonds have a short interaction distance and usually have a large strength. They can generally be classified into covalent bonds (including coordination bonds and metallic bonds in specific situations) and ionic bonds, and the interaction energy is generally several hundred kJ/mol. Weak interactions have a much longer action distance and are about one order of magnitude weaker than chemical bonds. They contain a wide variety of types, such as ordinary van der Waals (vdW) interactions,[1,2] hydrogen bonds (H-bonds),[3-5] halogen bonds,[6-8] chalcogen bonds,[9,10] pnicogen bonds,[11,12] tetrel bonds,[13,14] dihydrogen bonds,[15] regium bonds,[16,17] π-π interactions,[18,19] and their interaction energy is generally several to tens of kJ/mol. There are also some interactions between the two categories, such as the charged H-bond $[F\cdots H\cdots F]^-$,[20] which has a strong covalent nature with an interaction energy of as high as 274 kJ/mol.[3] The interactions can also be divided into covalent interaction and noncovalent interaction according to their nature, the ionic bonds and weak interactions of common strength collectively correspond to the latter. Whether and where various interactions exist in a chemical system, and what the nature they are, are always the issues of greatest concern to chemists. Studying these interactions is not only of great theoretical significance, but also of important practical significance.

Quantum chemistry is one of the most powerful and widely used methods for studying interactions in chemical systems today. Quantum chemical calculations can straightforwardly generate electron wavefunctions. According to the principles of quantum mechanics, the electron wavefunction contains all the information of the system. Wavefunction analysis is a general term for a large class of methods that transform the complex electron wavefunction into information with clear chemical and physical meanings. Compared with common theoretical approaches for studying interactions, such as structure optimization and energy calculations, wavefunction analysis provides key complementary insights into the characteristics of interactions. The field of wavefunction analysis encompasses a variety of three-dimensional real-space functions with different physical meanings and practical applications. Many analysis methods rely on real-space functions to examine chemical bonds and weak interactions, or covalent and noncovalent interactions, in different forms, including graphical analysis, topological analysis, basin analysis, domain analysis, and more.

The purpose of this review is to provide a comprehensive introduction to visualization-based analysis methods that utilize real-space functions. These methods transform the highly abstract electron wavefunction into intuitive images that are easy for chemists to understand. Many of these methods have been widely adopted in the literature due to their irreplaceable importance and have even become standard tools for studying interactions.

In Section 2 of this article, various methods for graphically displaying noncovalent interactions will be comprehensively reviewed, and Section 3 will introduce various visualization methods specifically designed for revealing covalent interactions. In addition, Section 4 will briefly mention the computer programs that can perform these analyses, especially the Multiwfn program[21,22] we have developed over the long term, which can conveniently and efficiently realize all the analysis methods described in this article.

2. Visual Analysis of Noncovalent Interactions

2.1 NCI method

The noncovalent interaction analysis method proposed by Yang and coworkers in 2010,[23] commonly referred to as the NCI or NCIplot method, is widely used to graphically reveal the regions and types of noncovalent interactions. Since the ideas and details of this method have been thoroughly introduced in the author's recent review,[24] only the key points of the NCI method are summarized in this section. The reduced density gradient (RDG) function is defined as follows[25]

$$\mathrm{RDG}(\mathbf{r}) = \frac{1}{2(3\pi^2)^{1/3}} \frac{|\nabla\rho(\mathbf{r})|}{\rho(\mathbf{r})^{4/3}} \tag{1}$$

where ρ is the electron density, $|\nabla\rho|$ is the gradient norm of the electron density, and $\mathbf{r}$ represents the position vector in three-dimensional real space. RDG is the dimensionless form of $|\nabla\rho|$ and appears in the definition of many exchange-correlation functionals. In the NCI method, RDG is used to display the regions where noncovalent interactions occur. Specifically, in low-density areas (usually $\rho < 0.05$ a.u.), the isosurface of RDG with an isovalue around 0.5 can satisfactorily exhibit the regions where noncovalent interactions predominantly occur in the system. Furthermore, to distinguish the types of weak interactions in different regions, the NCI method defines a function, $sign(\lambda_2)\rho$, where λ_2 is the second-largest eigenvalue of the electron density Hessian matrix, and $sign(\lambda_2)$ represents the sign of λ_2. The $sign(\lambda_2)\rho$ is mapped onto the RDG isosurfaces that describe noncovalent interactions, with different colors assigned according to the value. A larger ρ implies a stronger interaction. Positive and negative $sign(\lambda_2)$ indicate attractive and repulsive interactions, respectively. The introduction of $sign(\lambda_2)$ was inspired by the classification of bond critical points (BCPs) and ring critical points (RCPs) in the QTAIM theory:[26] BCPs often appear between atoms with attractive interactions, while RCPs typically appear within sterically hindered ring regions. The difference between BCPs and RCPs just depends on the sign of λ_2 at the corresponding position.

Since the NCI method relies solely on the electron density (and its first and second derivatives), which can be obtained through high-precision crystal diffraction, in principle, NCI analysis can be performed purely based on experimental data. However, since it is much more convenient to obtain the electron density of an isolated system through quantum chemistry calculations and that of a periodic system through first-principles calculations, and because the electron density obtained by combining the widely used and efficient density functional theory (DFT) with a medium-quality basis set is already of satisfactory quality, most NCI analyses in the literature are based on theoretically calculated electron densities.

As examples, Fig. 1 shows the NCI map for three representative systems involving noncovalent interactions. The interactions are revealed by the isosurfaces of RDG = 0.5, which are colored by $sign(\lambda_2)$ according to the color bar. The types of interactions that correspond to different color ranges are also indicated on the color bar. Fig. 1(a) shows a guanine-cytosine base pair adsorbed on circumcoronene. The three H-bonds between guanine and cytosine are clearly visible, represented by the small blue isosurfaces. The broad green isosurfaces between the base pair and circumcoronene unambiguously reveal the existence of a π-π stacking effect. The prominent steric effects within the five- and six-membered rings are vividly exhibited by the small red isosurfaces. Clearly, the NCI method successfully reveals all noncovalent interactions in this system. Fig. 1(b) shows the NCI map of $NaNO_3$. It can be seen that the two Na-O ionic bonds are reasonably exhibited by the two blue areas in the isosurface, and the red area in the center of the isosurface implies the steric effect caused by the close contact of Na···N. Fig. 1(c) shows the NCI map of the **4Cy**$_{\text{axax}}$ molecule,[27] which consists of two cyclohexanes connected by an acetylene bridge in a biaxial conformation. It has been pointed out that this conformation is notably stabilized by intramolecular dispersion interaction, making its electronic energy lower than that of other conformations.[27] Indeed, the NCI map clearly shows an evident green isosurface between the two cyclohexanes, reflecting the dispersion stabilization effect. Note that dispersion term corresponds to the attractive component of vdW interaction, while exchange-repulsion term corresponds to the repulsive component.[1,28]

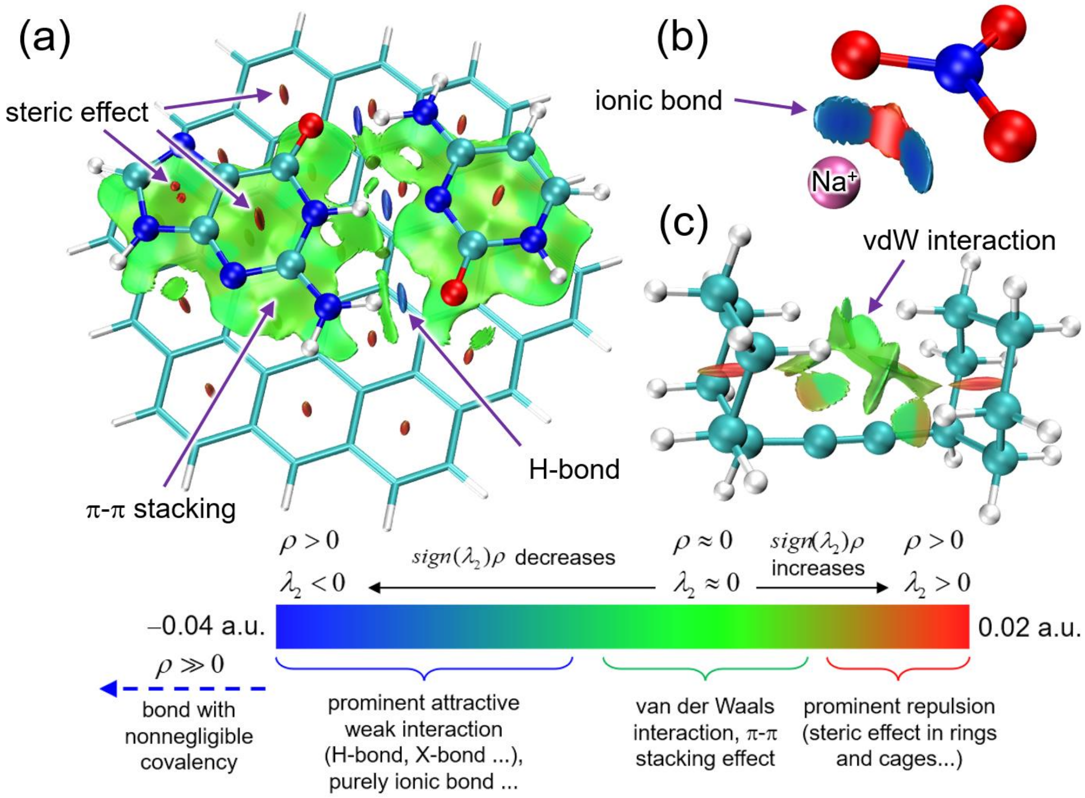

Figure 1 NCI maps of some representative systems. (a) Guanine-cytosine base pair adsorbed on circumcoronene. (b) $NaNO_3$ molecule. (c) **4Cy$_{\mathbf{axax}}$** molecule. The color bar of the mapped function $sign(\lambda_2)\rho$ is shown. White, cyan, blue, red and pink atoms correspond to hydrogen, carbon, nitrogen, oxygen and sodium, respectively, hereinafter.

González-Veloso et al. made full use of the NCI method to reveal noncovalent interactions in their study of the interaction between alkali metal ions and buckybowls,[29] which serves as an interesting application example (see Fig. 2). It is noteworthy that the $sign(\lambda_2)$ coloring method used in Fig. 1 is the most commonly employed in the literature; however, some papers, such as Ref. [29], use different color scale ranges for better image clarity or due to conventions. Therefore, the color bar should always be clearly provided in an NCI map. Additionally, Fig. 2 employs an RDG value of 0.55 to define the isosurfaces, which slightly differs from the RDG value used in Fig. 1. Fig. 2(a) shows the NCI map of complexes formed by different alkali metal cations and buckybowls. It can be seen that as the ionic radius increases from Li^+ to Cs^+, the area of their interaction with buckybowl P1 also increases significantly. However, as indicated by the complexation energy in parentheses, the interaction strength between the ions and P1 decreases from Li^+ to Cs^+, which is vividly reflected in the color of the isosurface changing from blue (relatively strong interaction) to green (very weak interaction). The underlying reason is that the polarization ability of alkali metal ions weakens progressively from Li^+ to Cs^+. Fig. 2(b) shows the NCI map of the complexes formed by Cs^+ and different buckybowls. It can be seen that as the buckybowl changes from the fully open P1 to the fully closed C_{60} fullerene, the complexation energy gradually shifts from a relatively negative value towards zero and ultimately becomes significantly positive. Correspondingly, under the small color scale range (-0.01 to 0.01 a.u.), the RDG isosurface changes from light blue to green, and then to red, intuitively reflecting that the steric hindrance becomes stronger and stronger, causing the interaction between Cs^+ and the buckybowl to shift from attractive to repulsive. This example demonstrates that the NCI visualization analysis can effectively exhibit the strength and characteristics of the interaction of interest.

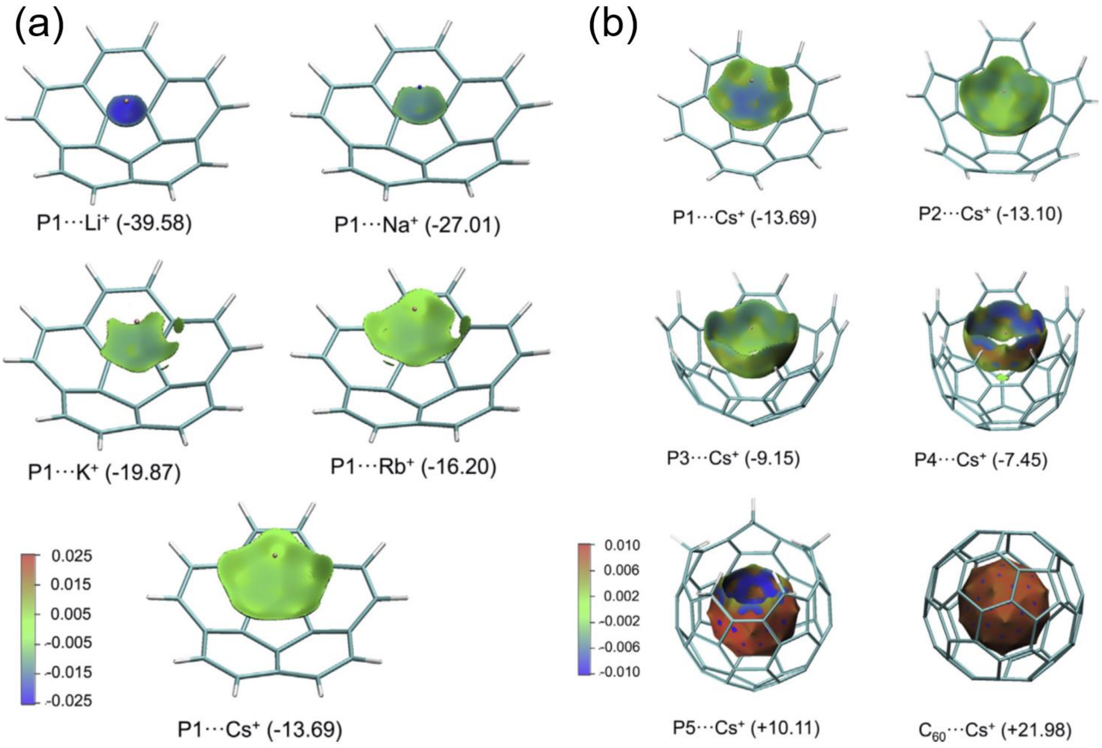

Figure 2 NCI map of complexes formed by (a) different alkali metal cations and buckybowl P1 (b) Cs^+ and different buckybowls. Complexation energies are given in parentheses (kcal/mol). The isosurfaces correspond to RDG of 0.55, and are colored according to the

respective color bar. Reprinted with permission from Ref. [29]. Copyright 2015 Elsevier.

The application of NCI analysis is not limited to isolated systems; it can also be used to study noncovalent interactions in periodic systems. For example, Fig. 3 shows the NCI map of a typical covalent organic framework compound, generated by the Multiwfn code based on the wavefunction obtained from periodic DFT calculations using the CP2K program.[30] The map fully illustrates the infinitely extended π-π interactions between the two layers, intralayer hydrogen bonds (blue areas), steric hindrance (dark brown and red areas), vdW interactions (green areas), and more.

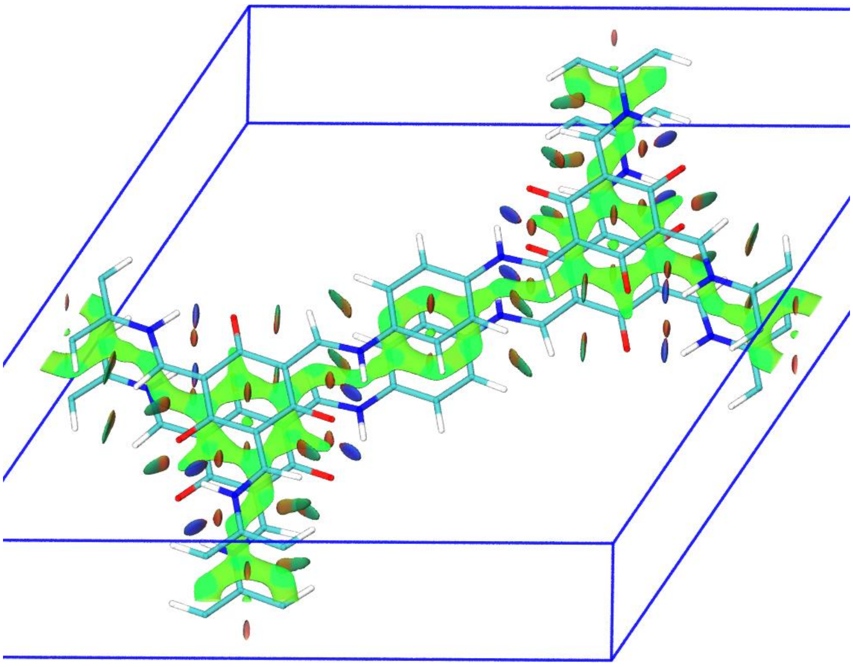

Figure 3 NCI map for a periodic COF system. The color bar of the mapped $sign(\lambda_2)\rho$ is the same as Fig. 1. The blue box highlights the cell involved in the periodic DFT calculation. For clarity, the periodicity in the direction perpendicular to the layers is ignored.

There are numerous other examples of the application of the NCI method in the literature. For instance, Ref. [31] used the NCI method to intuitively illustrate the adsorption of different small molecules by the novel cyclo[18]carbon molecule. In Ref. [32], the authors analyzed the intramolecular H-bonds of different configurations of benzo[a]pyrene diol epoxide using the NCI method and discussed the relative stability of the configurations. Additionally, many application examples can be found in review articles by us and others,[24,33] as well as in the original paper of the NCI method.[23] Our recent review also discusses some technical details of performing NCI analysis, such as the computational level required for electron density, the reasonable choice of grid spacing for calculating RDG and $sign(\lambda_2)$ grid data, and the proper preparation of geometry.

Some studies have attempted to expand the NCI analysis from a qualitative to a quantitative level. The general approach is to integrate a specific function, such as electronic kinetic density or $\rho^{4/3}$, within the isosurface of the NCI map to obtain the corresponding interaction energy.[24,34-38] However, this type of analysis has not been widely adopted due to issues related to universality and accuracy, although it is still worth further exploration.

The function mapped onto the RDG isosurface does not necessarily have to be $sign(\lambda_2)\rho$. For example, Barquera-Lozada et al. found that when potential energy density is mapped onto the RDG isosurface representing a π-π interaction, the interaction strength in different regions can be clearly distinguished by color,[38] which is not achievable when $sign(\lambda_2)\rho$ is used as the mapping function.

It is often challenging to perform NCI analysis on large systems, such as proteins, due to the high computational cost of generating wavefunctions and calculating the grid data for NCI. In such cases, the promolecular approximation version of NCI, referred to as $\mathrm{NCI}^{\mathrm{pro}}$, can be used.[23] In this method, the actual electron density of the system is replaced by the promolecular density, ρ^{pro}, which represents the superposition of the electron densities of the atoms constituting the system in their free state. This is equivalent to a zero-order approximation of the actual electron density, assuming no interaction between atoms that leads to electron density transfer or polarization. Since $\mathrm{NCI}^{\mathrm{pro}}$ depends only on the elements and atomic coordinates, its computational cost is relatively low, making it applicable to systems containing more than 1000 atoms. While the graphical quality and accuracy of the $\mathrm{NCI}^{\mathrm{pro}}$ map are somewhat lower than those of the NCI map due to the promolecular approximation, the weak interactions typically have little impact on the electron density. Therefore, if the focus is solely on weak interaction regions, the quality of the NCI^{pro} map is usually acceptable and closely resembles the NCI map. An example of NCI^{pro} analysis is shown in Fig. S4 of Ref. [22], where the prominent vdW interactions between the two α-helices of the protein glycophorin A are clearly displayed in the NCI^{pro} map.

2.2 IRI method: Expanding NCI analysis to all types of interactions

The NCI method cannot simultaneously reveal covalent and noncovalent interactions on an equal footing. To address this limitation, Chaudret et al. suggested combining the NCI map with the electron localization function (ELF) map,[39] as the latter can graphically display covalent interaction regions, which will be introduced later. However, it is obviously cumbersome to consider both analyses at the same time. Although the density overlap regions indicator (DORI) function can reveal both covalent and noncovalent interactions,[40] its definition is complex, and the graphical quality is often unsatisfactory, with isosurfaces typically appearing noisy and fragmented.

In 2021, we proposed the IRI analysis,[41] which is an extension of the NCI method. This approach can simultaneously display various types of interactions within a single map. The key difference between IRI and NCI analyses is that the former uses the isosurface of the IRI function instead of the RDG to display the main interaction regions. The definition of the IRI function is as follows:

$$\mathrm{IRI}(\mathbf{r}) = \frac{|\nabla\rho(\mathbf{r})|}{[\rho(\mathbf{r})]^{a}} \tag{2}$$

in which the parameter a was empirically chosen to be 1.1 to best balance the graphical representation of various kinds of interactions. Isosurface of IRI=1.0 a.u. is usually adopted in the IRI analysis, but it can be slightly adjusted to obtain a better representation for a specific system.

To illustrate the unique value of the IRI analysis, some typical examples are shown in Fig. 4. The isosurfaces and colors in the IRI map of zirconocene dichloride in Fig. 4(a) clearly reveal various interactions, such as C-C and C-H covalent bonds, coordination bonds, interligand steric hindrance, and vdW interactions. Because the electron density in the chemical bond regions is high, the corresponding isosurfaces are dark blue, according to the color bar (the same as Fig. 1). Fig. 4(b) shows the NCI map of a Te-containing chalcogen bond dimer, where the two noncovalent chalcogen bonds, the intermolecular steric effects caused by close contact, and all chemical bonds are clearly exhibited. Fig. 4(c) corresponds to a covalent dimer of nonacene, where the dark blue isosurfaces clearly reveal all covalent bonds, including those between the two nonacene molecules. Additionally, the significant steric effect caused by the covalent dimerization, as well as the large-area π-π stacking, are also visible. These three examples fully demonstrate the key advantage of IRI analysis over NCI analysis: it conveys much richer information. Therefore, we generally recommend using IRI over NCI.

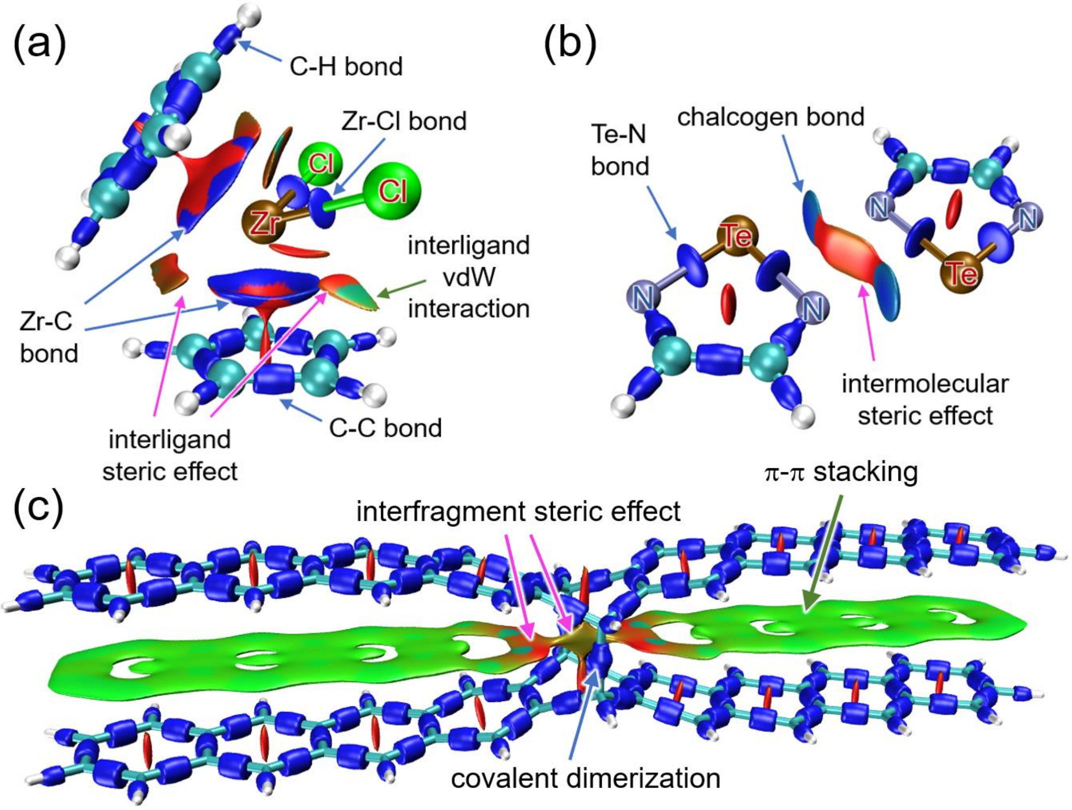

Figure 4 IRI maps of (a) zirconocene dichloride, (b) Te-containing chalcogen bond dimer, and (c) nonacene covalent dimer. The color bar of the mapped $sign(\lambda_2)\rho$ is the same as Fig. 1. Isovalue of IRI is set to 0.8 a.u. for (a) while 1.0 a.u. for (b) and (c) for best graphical effect. (a) and (b) are reprinted with permission from Ref. [24]. Copyright 2024 Elsevier.

Since IRI can display various interactions on an equal footing, it is ideal for revealing the variation in the strengths and types of interactions during structural changes. To illustrate this, Fig. 5 presents an example of using IRI analysis for a complete SN_2 reaction process. The supplementary material in Ref. [41] also provides an IRI animation of this reaction process, which more intuitively shows the changes in the IRI isosurface. From the IRI maps of some representative structures in the reaction process shown in the figure, it can be observed that at the beginning of the reaction, the green region of the isosurface between OH^- and CH_3CH_2Br indicates the formation of a weakly interacting complex. As the reaction progresses, the color of the isosurface between the O and C atoms becomes increasingly blue, clearly indicating that the attraction is strengthening. Eventually, an IRI isosurface with typical covalent bond characteristics is formed. Meanwhile, the C-Br bond that initially exists weakens gradually as the reaction continues, and by the end, only a large green isosurface remains between Br and C, reflecting the formation of a vdW complex between Br^- and ethanol. This example demonstrates that using IRI analysis to study chemical processes is highly effective for understanding the reaction mechanism. Additional examples of applying IRI to explore chemical reactions can be found in our review[24] and the original IRI paper.[41]

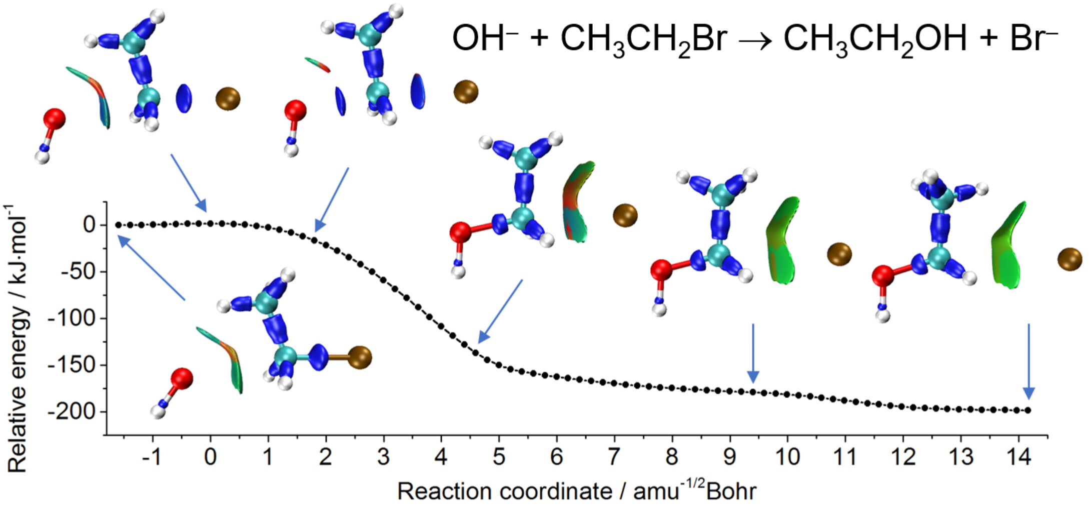

Figure 5 IRI map of some representative structures in a SN_2 substitution reaction process.

Isovalue of IRI is set to 0.95 a.u. The same color scale as Fig. 1 is used. Energy variation relative to the reactant complex is plotted as the curve. Reprinted with permission from Ref. [41]. Copyright 2021 John Wiley and Sons.

An important byproduct of the IRI analysis is the IRI-π analysis, which refers to the IRI analysis that considers only π-electrons.[41] This analysis can be conveniently performed with the help of our proposed algorithm for the automatic detection of π orbitals.[42] In this analysis, electron density is mapped onto the IRI-π isosurface, typically with an isovalue of 1.0 a.u. For systems involving π-interactions, the IRI-π analysis can distinguish both the type and strength of these interactions. It is well known that the C-C bonds in ethylene and acetylene have one and two sets of π-interactions, respectively. As shown in Figs. 6(a) and (b), their IRI-π images are quite distinct. The former shows two small, separated isosurfaces, while the latter displays a ring-shaped isosurface. Based on this difference, one can differentiate the characteristics of π-interactions in complex systems. Furthermore, by examining the magnitude of the electron density mapped onto the IRI-π isosurface, the strength of the same type of π-interactions can be compared. For example, a series of derivatives of cyclo[18]carbon, C_{18}-$(CO)_n$ (n = 2, 4, 6), was recently investigated by us,[43] the IRI-π map of C_{18}-$(CO)_2$ is shown in Fig. 6(c). From the shape of the isosurfaces in this map, one can easily observe that there is only a single set of π-interactions in the CO addition region, while double sets of π-interactions (in-plane and out-of-plane) are present in other regions, which is similar to the situation in pristine cyclo[18]carbon.[44] Additionally, as indicated by the purple arrows, the double sets of π-interactions on different C-C bonds exhibit notably different strengths. The relatively green and blue isosurfaces represent relatively low and high π-electron density in the corresponding regions, respectively, it is evident that the π-bond represented by the blue isosurface is significantly stronger than that represented by the green isosurface.

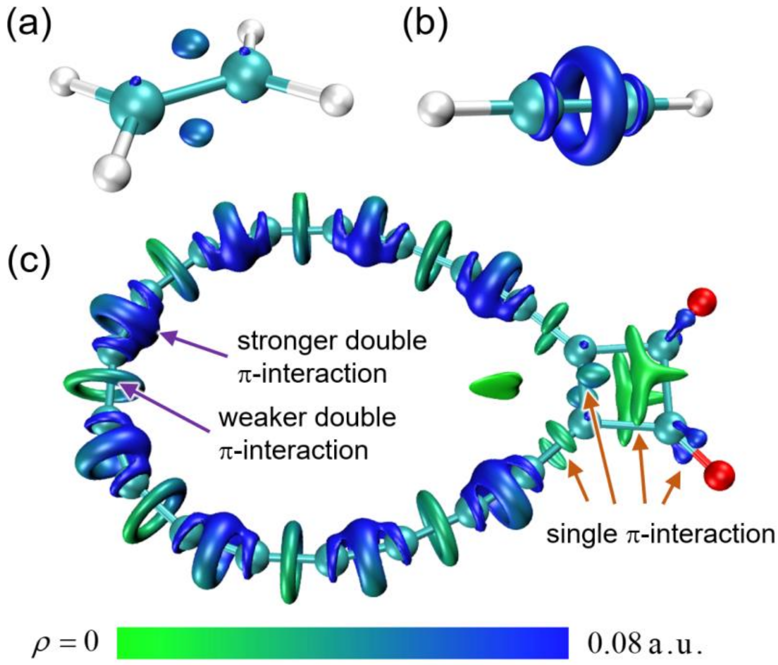

Figure 6 IRI-π maps of (a) ethene, (b) acetylene, and (c) C_{18}-$(CO)_6$. π-electron density is mapped onto the isosurfaces of IRI-π = 1.0 a.u. according to the color bar. (a) and (b) are reprinted with permission from Ref. [41]. Copyright 2021 John Wiley and Sons. (c) is adapted from Ref. [43].

Gao et al. reported the synthesis of a metalated carbyne ribbon,[45] as shown in Fig. 7. In this work, they nicely employed the IRI and IRI-π analyses to examine the interactions within the system. The IRI isosurface map and plane map in Figs. 7(a) and 7(b) clearly depict the weak interaction regions between the ribbons and the chemical bond regions within each ribbon. Additionally, significant IRI-π values are observed between the ribbons (Figs. 7(c) and 7(d)), confirming that the ribbons are assembled through π-π stacking interactions. Furthermore, the circular isosurfaces around the Cu atoms suggest the possibility of π-interactions between the Cu and carbon atoms.

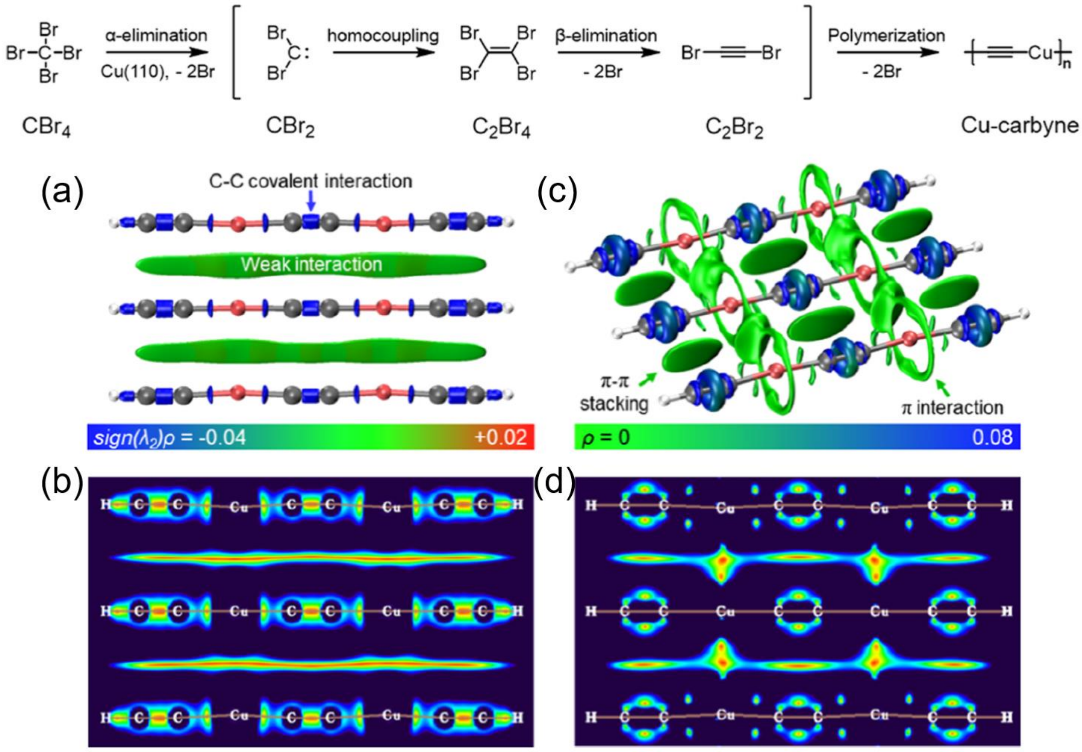

Figure 7 IRI and IRI-π maps of Cu-carbyne. (a) and (c) are colored isosurface maps, (b) and (d) are the corresponding color-filled plane maps. Reprinted with permission from Ref. [45]. Copyright 2023 American Chemical Society.

2.2 IGM, IGMH, and mIGM: Fragment-based visual analysis methods

The independent gradient model (IGM), proposed in 2017, is another highly valuable branch of visual analysis methods.[46] In principle, it can be applied to study any type of interaction, much like the IRI method, but it has primarily been used for investigating noncovalent interactions in the literature. Since the underlying concept and implementation of the IGM method have already been thoroughly described in Refs. [24] and [47], only the key aspects of this method are outlined here.

The IGM method defines a function $\delta g(\mathbf{r}) = g^{\mathrm{IGM}}(\mathbf{r}) - g(\mathbf{r})$, where g represents the gradient norm of the promolecular density, and g^{IGM} represents the gradient norm of IGM type. It is defined in such a way that the density gradients of free-state atoms do not cancel each other out due to different signs when summed. Mathematically, these functions can be expressed as:

$$\begin{aligned} g(\mathbf{r}) &= \left| \sum_i \nabla \rho_i^{\text{free}}(\mathbf{r}) \right| \\ g^{\text{IGM}}(\mathbf{r}) &= \sum_i \left| \nabla \rho_i^{\text{free}}(\mathbf{r}) \right| \end{aligned} \tag{3}$$

In this context, ρ_i^{free} represents the spherically averaged density of atom i in its free state, with i looping over all atoms in the system. It has been found that the isosurfaces of δg can reasonably reveal regions where prominent interatomic interactions occur. Unlike NCI and IRI, δg offers a controllable display of interactions with varying strengths. Generally, the stronger the interaction, the larger the δg value in the corresponding region. Due to this feature, when a large isovalue of δg is used, only strong interactions are revealed, whereas a small isovalue can display both strong and weak interactions. Additionally, IGM defines δg^{inter} and δg^{intra} functions, allowing for the separate display of interfragment and intrafragment interactions:

$$\begin{aligned} \delta g^{\text{inter}}(\mathbf{r}) &= g^{\text{IGM,inter}}(\mathbf{r}) - g^{\text{inter}}(\mathbf{r}) \\ \delta g^{\text{intra}}(\mathbf{r}) &= \delta g(\mathbf{r}) - \delta g^{\text{inter}}(\mathbf{r}) \end{aligned} \tag{4}$$

where

$$\begin{aligned} g^{\text{IGM,inter}}(\mathbf{r}) &= \sum_A \left| \sum_{i \in A} \nabla \rho_i^{\text{free}}(\mathbf{r}) \right| \\ g^{\text{inter}}(\mathbf{r}) &= \left| \sum_A \sum_{i \in A} \nabla \rho_i^{\text{free}}(\mathbf{r}) \right| \end{aligned} \tag{5}$$

with A and i being the index of fragments and atoms, respectively. Two or more fragments can be defined based on actual needs. IGM employs $sign(\lambda_2)\rho$ to color δg or δg^{inter} or δg^{intra} isosurfaces to distinguish the interaction strengths and types, which is in analogy with NCI and IRI.

A key drawback of the IGM method is that its isosurfaces are usually quite bulgy, which not only hinders visual analysis but may also cause unreasonable coloring of the isosurfaces. This occurs because the isosurfaces are often over-extended to areas very close to the nuclei, where electron density is much higher than in the interatomic interaction regions. To address this issue, we proposed a variant of the IGM method called IGM based on the Hirshfeld partition of molecular electron density

(IGMH),[47,48] which has been widely employed in the literature in recent years. In this method, the density of free-state atoms in Eqs. (3) and (5) is replaced by the atomic electron density $\rho_i^{\mathrm{IGMH}}(\mathbf{r}) = \rho(\mathbf{r})w_i(\mathbf{r})$, where ρ is the actual electron density of the system, and $w_i(\mathbf{r}) = \rho_i^{\mathrm{free}}/\rho^{\mathrm{pro}}$ is the Hirshfeld atomic weighting function.[49,50] Additionally, the derivative of ρ_i^{IGMH} with respect to the Cartesian components, which is needed in the IGMH analysis, is evaluated in a specific way.[48] It should be noted that there is another approach to realizing IGM analysis based on the actual electron density, which involves the gradient-based partition (GBP) scheme,[51] referred to as IGM(GBP). However, the principle of IGM(GBP) is more complicated and has not become as popular as IGMH.

To illustrate the differences between IGM, IGMH, and NCI, Fig. 8 presents an example: the trimer of capped phenylalanine.[52] In both the IGM and IGMH analyses, the isosurfaces correspond to $\delta g^{\mathrm{inter}} = 0.0035\ \mathrm{a.u.}$, and each of the three molecules is defined as a fragment, so the maps reveal only intermolecular interactions. It can be seen that the IGMH map perfectly exhibits all types of interactions between the three molecules, including vdW interactions and N-H⋯C H-bond interactions. In comparison, although the IGM map also shows the same information, the isosurfaces are quite bulgy, making the visual effect clearly inferior to the IGMH map. Moreover, as indicated by the purple arrows in the map, some areas of the IGM isosurfaces have obviously unreasonable coloring—blue and orange colors appear on isosurfaces in areas that should correspond to vdW interactions, which could mislead researchers. Since the NCI map simultaneously shows both intramolecular and intermolecular interactions, and the isosurfaces are relatively scattered, the image is clearly not as easy to analyze as the IGMH map. Additionally, although the grid spacing used to plot these maps is already small (0.15 Bohr), some isosurfaces in the NCI map, such as the one indicated by the orange arrow, appear jagged, while the isosurfaces in the IGMH and IGM maps do not have this issue. This simple example highlights the clear advantages of IGMH over NCI: the fragments in the IGMH analysis can be appropriately defined according to the specific purpose of the study, allowing for a focused examination of interactions in the region of interest, and the requirement for grid spacing is significantly lower than in NCI. Considering that the computational cost of IGMH is similar to that of NCI and IRI, IGMH is the optimal choice for researchers interested in interactions between or within specific fragments.

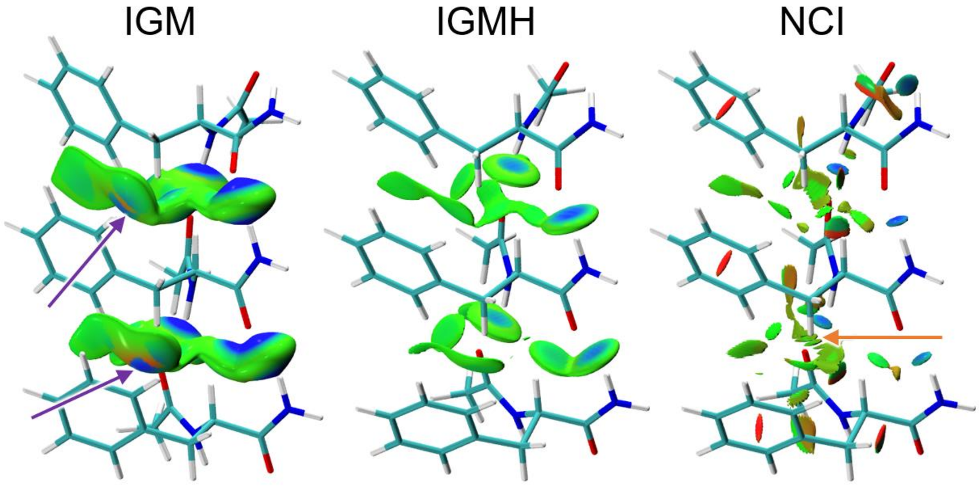

Figure 8 IGM, IGMH and NCI maps of trimer of capped phenylalanine. Each monomer is defined as a fragment in the IGM and IGMH analyses. The isosurfaces in the IGM and IGMH maps correspond to $\delta g^{\mathrm{inter}}$ of 0.0035 a.u., the isosurfaces in the NCI map correspond to RDG of 0.5. The isosurfaces are colored according to the color bar in Fig. 1, but for IGM and IGMH, color scale range of -0.05 to 0.05 a.u. is used instead. Reprinted with permission from Ref. [52].

The complexation between cyclocarbons and fullerenes was thoroughly studied by Liu and Lu very recently.[19] One of the research topics focused on examining how the interaction between two cyclocarbons and a fullerene changes with the size of the cyclocarbons, IGMH analysis was employed to visually characterize the intermolecular interactions in the trimers, as shown in Fig. 9. For clarity, the $\delta g^{\mathrm{inter}}$ isosurfaces corresponding to the cyclocarbon-fullerene and cyclocarbon-cyclocarbon interactions are colored yellow and green, respectively. From the figure, it can be observed that as the size of the cyclocarbons increases, the area of the yellow isosurfaces gradually increases, directly suggesting that the cyclocarbon-fullerene π-π interaction strengthens. For C_n@C_{60} with n ranging from 18 to 30, the green isosurface occupies only a small area, indicating that the π-π interaction between the cyclocarbons is present but very weak. In the structure of $2C_{34}@C_{60}$, a circular green isosurface with wide coverage appears between the two cyclocarbons, clearly indicating a very strong π-π stacking effect, which also implies that this trimer is highly stable. Indeed, the above speculations based on IGMH analysis are well supported by the interfragment interaction energies calculated using high-precision quantum chemical methods. Additionally, the study found that the area of the $\delta g^{\mathrm{inter}}$ isosurface describing the π-π interaction has an ideal linear relationship with the interaction energy between the interacting parts.

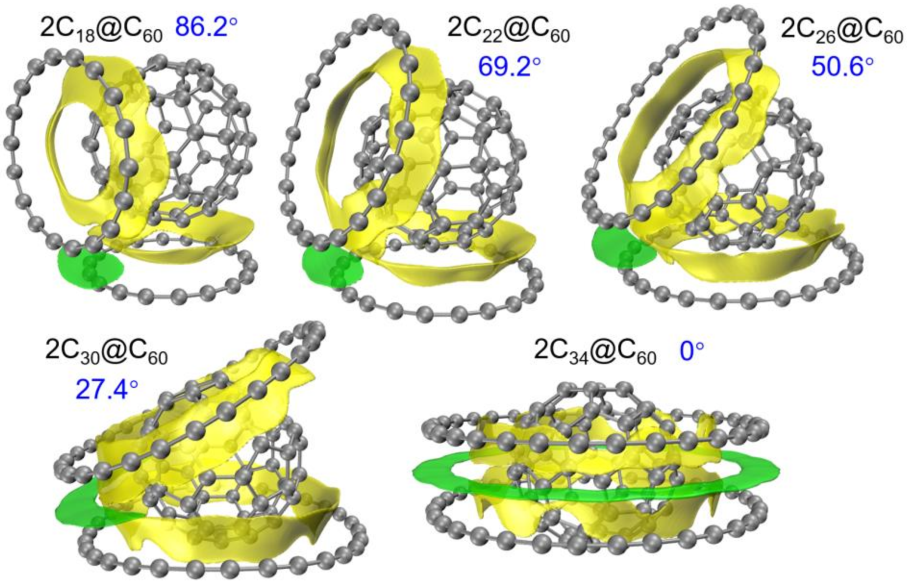

Figure 9 IGMH maps of complexes formed by two cyclocarbons and a C_{60} fullerene. Each monomer is defined as a fragment in the IGMH analysis. The isosurfaces correspond to $\delta g^{\mathrm{inter}}$ of 0.003 a.u. The isosurfaces representing cyclocarbon-fullerene and cyclocarbon-cyclocarbon π-π interactions are colored by yellow and green, respectively. The blue texts denote the angle between the two cyclocarbons. Adapted from Ref. [19].

Another excellent application of IGMH is the work of Zheng and coworkers.[53] They applied IGMH analysis to two chiral transition state structures and carefully examined and compared the differences in noncovalent interactions between them, successfully explaining how the asymmetric catalytic effect is influenced by intermolecular interactions.

IGMH is also highly useful and convenient for visually investigating interactions in crystals or on solid surfaces. When using IGMH to study interactions in molecular crystals, the best approach is often to use a cluster model. This involves extracting a cluster containing a central molecule and a shell of neighboring molecules from the crystal, performing quantum chemical calculations to obtain the required wavefunction, and then defining the central molecule and the surrounding ones as separate fragments in the IGMH analysis. Fig. 10(a) illustrates this approach for analyzing interactions in urea crystals. It can be seen that the IGMH map clearly shows the multiple hydrogen bonds between urea molecules (represented by blue isosurfaces in the central area) and the evident vdW interactions (depicted by completely green isosurfaces).

IGMH can also be applied directly to the wavefunctions obtained from periodic first-principles calculations, avoiding the need to extract a proper cluster and manage boundary effects. Fig. 10(b) demonstrates this approach, where the system consists of a toluene adsorbed in a zeolite cavity. The toluene and zeolite moieties are defined as separate fragments in the analysis. This figure intuitively shows where the vdW interaction between toluene and zeolite primarily occurs, providing valuable insight into interpreting adsorption experiment results from a microscopic perspective and in the theoretical design of pore structures for the selective adsorption of specific substances.

It is noteworthy that Su et al. used IGMH to study the interactions between open-cage fullerene derivatives in a synthesized single crystal, which is another mice example of applying IGMH to crystal systems.[54]

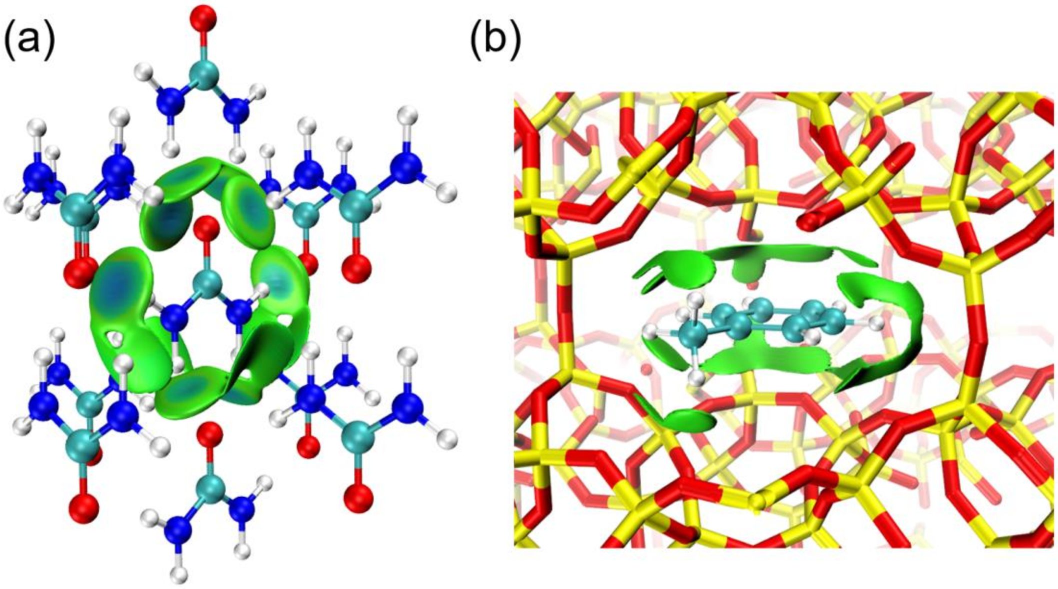

Figure 10 IGMH maps showing (a) interactions between urea molecules in crystal environment, and (b) interactions between an adsorbed toluene and zeolite. The isosurfaces in (a) and (b) correspond to $\delta g^{\mathrm{inter}}$ of 0.004 and 0.005 a.u., respectively. The coloring method is the same as Fig. 1 but with range of -0.05 to 0.05 a.u. (b) is reprinted with permission from Ref. [47]. Copyright 2022 John Wiley and Sons.

Another advantage of IGMH over NCI and IRI is that it defines quantitative indices to measure the contribution of atoms and atom pairs to the interactions shown in the IGMH map.[47] Although these indices are very simple and may not have a direct positive correlation with the contribution to the interaction energy, they can still be used to identify which atoms and atom pairs are relatively important and therefore worthy of attention. Specifically, δG^{pair} is used to quantify the contribution of an atom pair to the interaction between two specific fragments, A and B:

$$\delta G_{i,j}^{\mathrm{pair}} = \int \delta g_{i,j}(\mathbf{r})\,\mathrm{d}\mathbf{r} \quad i \in A, j \in B \tag{6}$$

Percentage atom pair contribution is expressed as

$$\delta G_{i,j}^{\mathrm{pair}}(\%) = \frac{\delta G_{i,j}^{\mathrm{pair}}}{\sum_{k\in A}\sum_{l\in B}\delta G_{k,l}^{\mathrm{pair}}} \times 100\% \tag{7}$$

Contribution of atom i in fragment A to the interaction between fragments A and B is characterized by δG^{atom}

$$\delta G_{i}^{\mathrm{atom}} = \sum_{j\in B}\delta G_{i,j}^{\mathrm{pair}} \tag{8}$$

and δG^{atom}(%) corresponds to normalized δG^{atom}, which quantifies percentage contribution of an atom

$$\delta G_i^{\text{atom}}(\%) = \frac{\delta G_i^{\text{atom}}}{\sum_{j \in A} \delta G_j^{\text{atom}}} \times 100\% \tag{9}$$

Very similar idea has also been given by Ponce-Vargas et al. based on IGM.[55] In addition, Hénon et al. defined intrinsic bond strength index (IBSI) based on δG^{pair} of IGM(GBP) and bond lengths.[56] It is shown that IBSI is closely related to force constant, which is generally regarded as a reliable metric of intrinsic bond strength.

The atoms in the IGMH map can be colored by δG^{atom} or δG^{atom}(%) to help researchers easily identify the atoms that play a key role in the exhibited interactions. Fig. 11 provides an illustrative example, showing the intermolecular interactions of a triply interlocked covalent organic cage.[47] From Fig. 11(a), one can clearly observe all intermolecular common vdW interactions as well as the π-π stacking in the center of the dimer. Furthermore, Fig. 11(b) presents the structure map colored by δG^{atom} indices, which graphically highlights the relative importance of various atoms in the intermolecular interactions. Specifically, the redder (bluer) the color, the larger (smaller) the contribution of the atom to the interactions. It is evident that the atoms directly participating in the π-π stacking contribute the most, while contributions from other atoms around the center of the dimer are also notable. Most boundary atoms in the system contribute little to the interactions.

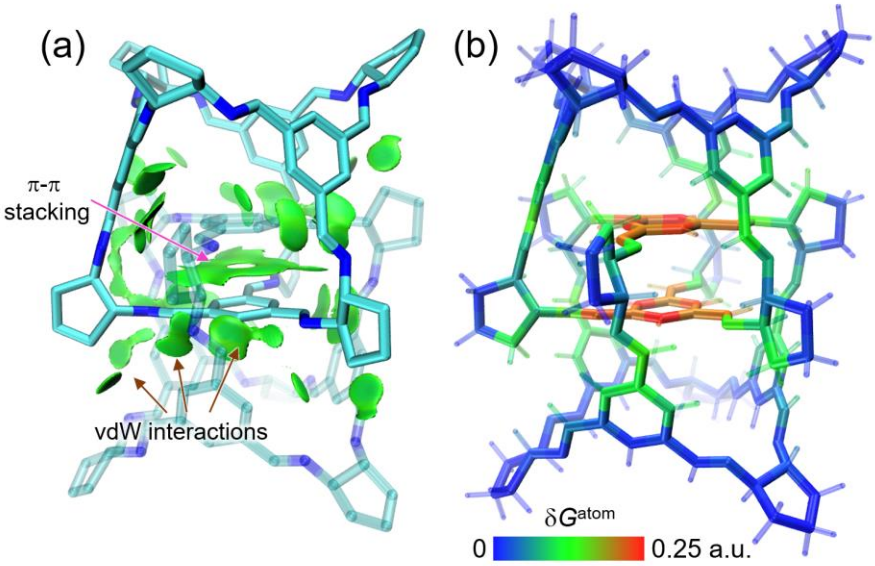

Figure 11 (a) IGMH map showing intermolecular interactions of a triply interlocked covalent organic cage, each molecule is defined as a fragment in the IGMH analysis. The first and second molecule are plotted in opaque and transparent styles, respectively. Isovalue of δg^{inter} of 0.004 a.u. is used, the coloring method is the same as Fig. 1 but with range of -0.05 to 0.05 a.u. (b) δG^{atom} colored structure map, hydrogens are drawn in transparent style for clarity. Reprinted with permission from Ref. [47]. Copyright 2022 John Wiley and Sons.

QTAIM is a classic and widely employed theoretical framework for studying chemical bonds and weak interactions, with topology analysis being one of its main approaches.[26,57] The BCP (bond critical point) generated by topology analysis is typically the most representative position for describing the interaction between atoms. Starting from a BCP, the bond path corresponding to the steepest ascent path of electron density can be considered the most representative path of the interaction between atoms. The properties of the BCP are closely related to the characteristics of the interaction.[58-60] It is important to note that methods like IGMH, IRI, and NCI are never merely graphical extensions of QTAIM analysis, as they can reveal many notable interactions that QTAIM cannot study, such as many intramolecular H-bonds.[61] For detailed relevant mathematical analysis and discussion, see Ref. [41]. The visual analysis methods mentioned above are not in conflict with QTAIM topology analysis. Since QTAIM focuses more on quantitative research based on the properties of BCPs, combining the two types of analysis provides complementary information. This allows for a more comprehensive and thorough understanding of the interactions, facilitating more accurate horizontal comparisons.

Fig. 12 shows an example from Ref. [21], which examines the intermolecular interaction of a H-bond dimer. In addition to the standard IGMH map, this figure also shows all the bond paths and BCPs between the two molecules. There are a total of six H-bonds between the molecules, each corresponding to a bond path and a BCP. The electron density at the BCP of each hydrogen bond is marked on the figure. From the IGMH map, it is clear that H-bonds 2 to 5 are stronger than H-bonds 1 and 6, as the centers of the isosurfaces of the former are blue, while those of the latter are completely green. However, it is difficult to distinguish which of H-bonds 2 to 5 is stronger simply by visualizing the color of the isosurfaces. Since the electron density at the BCP has been shown to correlate positively with hydrogen bond interaction energy,[3] the order of H-bond strength can be accurately determined as 2≈5>3≥4>1≥6 based on the marked electron density at the BCPs. This example demonstrates that combining visual analysis methods such as IGMH with the quantitative analysis in the QTAIM framework can be highly beneficial.

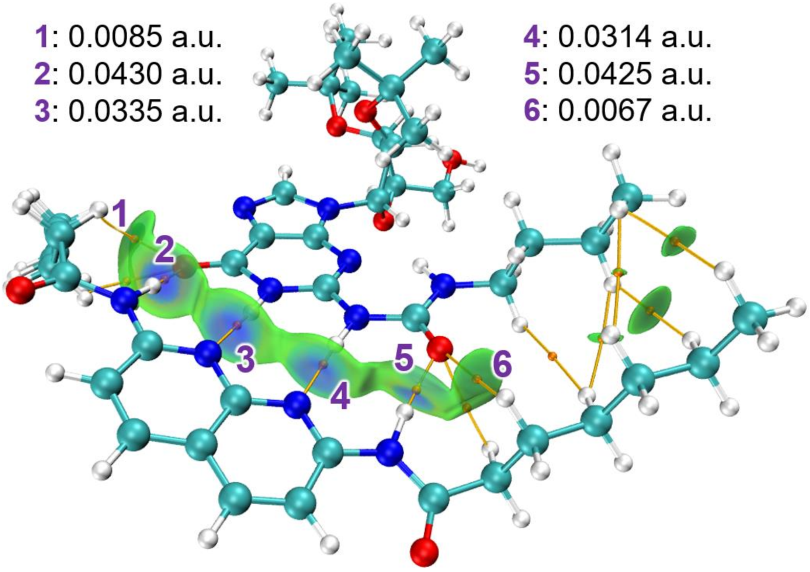

Figure 12 IGMH map showing intermolecular interactions of a H-bond dimer. Each monomer is defined as a fragment in the IGMH analysis. Isovalue of $\delta g^{\mathrm{inter}}$ of 0.004 a.u. is used, the coloring method is the same as Fig. 1 but with range of -0.05 to 0.05 a.u. Bond paths (golden curves) and BCP (small orange spheres) between the two monomers are also shown.

Electron densities at the BCPs corresponding to the six H-bonds are given for ease of quantitative comparison. Adapted from Ref. [21].

Since IGMH, like NCI and IRI, relies on the actual electron density, it can be too computationally expensive for systems with a very large number of atoms. On the other hand, the image quality of IGM, which is much less computationally demanding, is not ideal. This challenge led us to develop a method that balances the computational efficiency of IGM with an image quality similar to that of IGMH. The recently proposed modified IGM (mIGM) method achieves this goal ideally.[52] The concept behind mIGM is straightforward: it replaces the actual electron density used in IGMH with promolecular density. As a result, the relationship between mIGM and IGMH mirrors the relationship between $\mathrm{NCI}^{\mathrm{pro}}$ and NCI. The computational time for mIGM is comparable to that of IGM, and both methods only require the file containing atomic coordinates as input. It has been found that, at least for studying weak interactions, the image quality of mIGM is very close to that of IGMH and significantly better than IGM. For details, please refer to the comparisons and examples provided in Ref. [52]. Therefore, when investigating weak interactions between fragments and when IGMH analysis is impractical due to high computational costs, mIGM is an excellent alternative.

2.3 aNCI, aIGM, and amIGM methods: Analyzing noncovalent interactions in dynamic environments

In reality, due to the thermal motion of atoms, the relative positions of atoms are constantly changing. As a result, during a dynamic process, the interaction characteristics at each moment in the system will vary to some extent. The well-established molecular dynamics (MD) technology can easily simulate the real motion behavior of atoms, even in complex systems.[62] While the visualization analyses mentioned above can be performed at regular intervals to understand the weak interactions occurring in a real dynamic environment, comprehensively understanding these interactions from a large number of images is undoubtedly very challenging. To address this issue and intuitively display the interactions that occur during a dynamic process, Yang et al. proposed an extension of NCI analysis called the averaged NCI (aNCI) method in 2013.[63] In this method, the time-averaged electron density ($\bar{\rho}$) and its derivatives, generated over a period of MD simulation, are substituted into the calculation formulas of RDG and $sign(\lambda_2)\rho$ to yield averaged RDG (aRDG) and averaged $sign(\lambda_2)\rho$ ($sign(\bar{\lambda}_2)\bar{\rho}$). The $sign(\bar{\lambda}_2)\bar{\rho}$ colored aRDG isosurfaces can then reflect the average interactions occurring during the dynamic process. Additionally, this method defines the thermal fluctuation index, which vividly reflects the stability of noncovalent interactions at different locations during the dynamic process by mapping it onto the averaged RDG isosurface. Practical application examples can be found in its original paper, as well as in Refs. [24,64-66].

In principle, the $\bar{\rho}$ used by aNCI can be generated from the ρ^{pro} of each frame of the MD simulation based on classical force fields or the accurate density of each frame in an *ab-initio* MD simulation. Since the latter is very time-consuming, aNCI is typically used in combination with forcefield-based MD simulations. More technical details about aNCI, as well as guidance on how to prepare an appropriate MD trajectory for the analysis, can be found in our recent review.[24]

Here we will not introduce the aNCI analysis in more detail or give examples, because aNCI has several notable shortcomings in practical applications: (1) It requires a relatively fine grid quality; otherwise, the image will be noticeably jagged, much like the NCI map.[24] (2) It may fail to display certain interactions in some systems and sometimes generates isosurfaces that are difficult to interpret meaningfully.[52] (3) A large number of noisy isosurfaces often appear in regions of no interest, so a proper grid data screening process is almost always necessary to obtain an acceptable aNCI map. However, this screening is not only cumbersome but also somewhat arbitrary.

To address these issues with aNCI, we recently proposed the aIGM and amIGM methods, which extend IGM and mIGM to dynamic environment analysis, respectively.[52] In these methods, nonnegligible interfragment interactions are revealed by isosurfaces of averaged $\delta g^{\mathrm{inter}}$ ($\delta \bar{g}^{\mathrm{inter}}$), which is simply the time average of the $\delta g^{\mathrm{inter}}$ calculated for each frame of an MD trajectory. The $sign(\bar{\lambda}_2)\bar{\rho}$ is used to color the isosurfaces of $\delta \bar{g}^{\mathrm{inter}}$, similar to the aNCI method. The only difference between aIGM and amIGM lies in the method used to calculate the grid data for $\delta g^{\mathrm{inter}}$ in each considered frame—the former employs IGM, while the latter uses mIGM. We recommend using amIGM over aIGM because the isosurface of aIGM inherits the drawback of IGM: it is too bulgy. Compared with the aNCI method, amIGM has the advantage of visualizing only the average interactions between fragments of interest by properly defining the fragments. Moreover, it has lower requirements for grid quality and can still perform well in cases where aNCI results are poor.[52]

Fig. 13(a) presents a graphical representation of the average interaction between water and phenol in a system containing a phenol molecule dissolved in water, using amIGM.[52] The analysis considered 1000 frames from an MD simulation trajectory. The MD simulation was conducted at room temperature using the GAFF forcefield and the SPC/E water model. A phenol molecule was fixed in the center of the simulation box, and 443 water molecules filled the rest of the box. It can be observed that when the isovalue of $\delta \bar{g}^{\mathrm{inter}}$ is large, only the strongest average interactions between phenol and water are displayed. Specifically, the hydroxyl group of phenol simultaneously acts as both a H-bond donor and acceptor with surrounding water molecules. As the isovalue decreases to 0.003 a.u., slightly weaker interactions, such as π-H bonds, become visible, represented by isosurfaces above and below the six-membered ring. When the isovalue is further reduced to 0.0018 a.u., isosurfaces corresponding to the weakest vdW interactions between phenol and water become apparent. This example demonstrates that the amIGM isosurfaces are particularly effective for intuitively examining interactions. By properly adjusting the isovalue, the exhibition of interactions can be precisely controlled, and the distribution of isosurfaces aligns with the molecular symmetry, underscoring the reasonableness and unique advantages of the amIGM method. Additional application examples of amIGM, such as protein-ligand interactions and the shuttle motion of fullerene in a carbon nanotube, can be found in Ref. [52] and are recommended for interested readers.

For comparison, Fig. 13(b) presents the mIGM map for a randomly selected frame from the MD simulation. It is evident that the isosurface distribution in this case is significantly inconsistent with the molecular symmetry and is clearly inadequate for fully describing the interactions between phenol and water that occurred during the whole MD simulation. This highlights the importance of considering time-averaged results when studying interactions in dynamic processes.

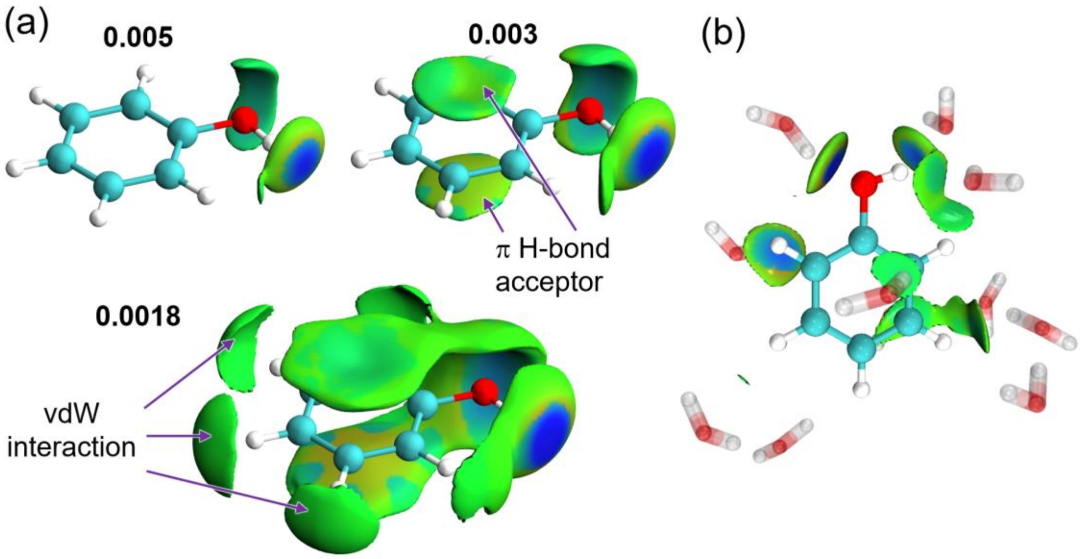

Figure 13 (a) amIGM maps with different $\delta\bar{g}^{\text{inter}}$ isovalues (bolded texts) showing the average intermolecular interactions of a solvated phenol and aqueous environment during a period of MD simulation. The phenol and all waters in the simulation box are defined as the two fragments for the amIGM analysis. $sign(\bar{\lambda}_2)\bar{\rho}$ is mapped onto the $\delta\bar{g}^{\text{inter}}$ isosurfaces using the same coloring method in Fig. 1 but with range of -0.05 to 0.05 a.u. Reprinted from Ref. [52] with permission. (b) mIGM map for a randomly selected frame from the MD trajectory, waters are shown in transparent style if any of its atom is within 3 Å of the phenol.

Many weak interaction visualization methods have been introduced above. To help readers clearly understand the relationships between them, Scheme 1 summarizes the derivative connections.

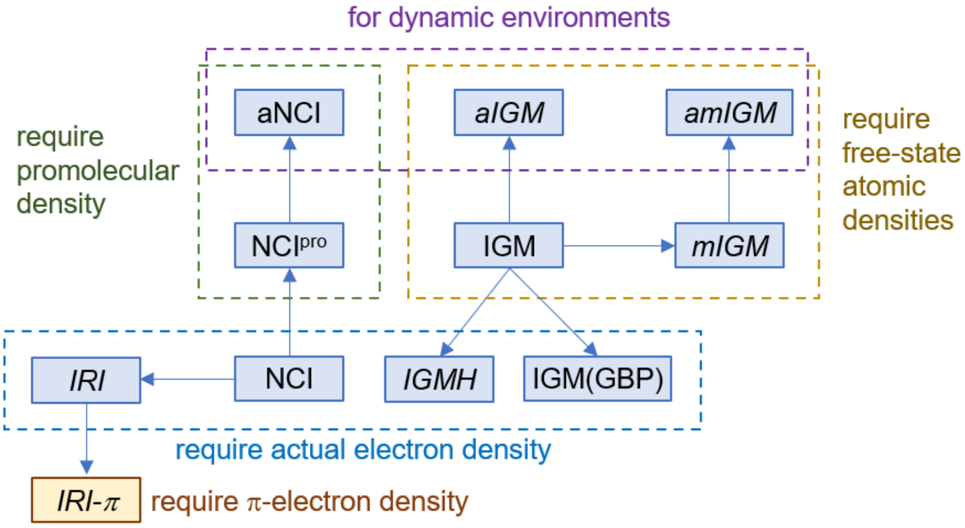

Scheme 1 Derivative relationship between various visual analysis methods. The names in italics are methods proposed by the present author. Note that the aNCI analysis can also be conducted based on actual electron density, but it is rarely used in this way because it is usually too expensive.

2.4 Other methods

There are several other methods for visually studying weak interactions, which differ significantly in their underlying principles from those introduced earlier. Due to space constraints, this section provides only a brief overview. Readers interested in a more detailed understanding are encouraged to consult the relevant literature and reviews.

2.4.1 Hirshfeld and Becke surface analyses

Hirshfeld surface analysis (HSA) is a widely used method for graphically visualizing interactions in molecular crystals,[67-69] though it can also be applied to molecular complexes. Its representation of interactions is somewhat complementary to the IGMH analysis described earlier. In essence, HSA employs the Hirshfeld partitioning method to compute a weighting function for each molecule based on atomic coordinates. This weighting function is a smooth three-dimensional function, with the sum of all molecular weighting functions equaling 1 at every point. By mapping specific properties, such as ρ^{pro} or normalized contact distance (d_{norm}), onto the isosurface of a molecule where the Hirshfeld weight function equals 0.5, researchers can intuitively examine the full range of interactions between the molecule and its surrounding environment. For a more detailed discussion, readers may refer to the review by Spackman et al.[68] Additionally, we have extended HSA to Becke surface analysis, which replaces the Hirshfeld weighting function with the Becke weighting function.[21] A key advantage of Becke surface analysis is its applicability in all cases, whereas Hirshfeld surfaces cannot be generated in regions where electron density is zero (i.e., far from any atom).

Fig. 14(a) presents a representative application of HSA by Irii and coworkers,[70] illustrating the Hirshfeld surface mapped with d_{norm} for the *p*CP-*t*Bu crystal at atmospheric pressure and at 3.3 GPa. This visualization clearly depicts intermolecular contacts, with redder regions indicating shorter contact distances and stronger interactions, while bluer regions represent longer distances and weaker interactions. At atmospheric pressure, the red areas highlight two H-bond sites, while white regions reveal intermolecular vdW and π-π interactions. Under 3.3 GPa, more areas shift toward white or red, indicating that the high pressure brings molecules closer together and enhances intermolecular interactions.

Fig. 14(b) provides an example of Becke surface analysis applied to a DNA double helix. Here, the Becke surface of one DNA strand is positioned precisely between the two strands, and the mapped ρ^{pro} vividly highlights the regions where hydrogen bonding occurs between base pairs. Notably, these H-bonds can also be effectively visualized using IGM or mIGM mapping, as demonstrated in Fig. 12 of Ref. [24].

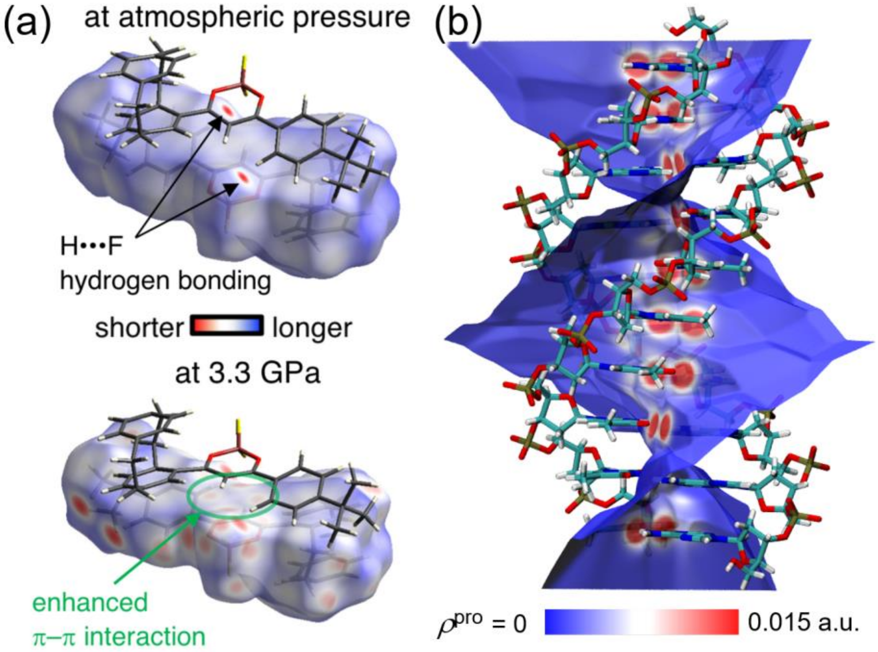

Figure 14 (a) Hirshfeld surface analysis maps of *p*CP-*t*Bu crystal at atmospheric pressure and at 3.3 GPa. The surfaces are mapped by d_{norm} according to the color bar. Reprinted with permission from Ref. [70]. Copyright 2022 Elsevier. (b) Becke surface analysis map of DNA double helix, promolecular density is mapped to the surface. Reprinted with permission from Ref. [21]. Copyright 2024 AIP Publishing.

2.4.2 ESP analysis

The electrostatic potential (ESP) is a real-space function that depends on the positions of nuclei and the distribution of electron density. The ESP at a given point **r** characterizes the electrostatic interaction energy between a unit charge placed at **r** and the present system, without accounting for charge transfer and polarization effects. Numerous excellent reviews on ESP are available,[71-75] so we will not elaborate on its fundamental concepts and applications in detail here. Instead, we will briefly highlight its significance in visually representing noncovalent interactions within molecular complexes.

Molecules tend to interact by complementing the signs of their ESP values, a principle known as the ESP complementarity rule, which helps maximize electrostatic attraction.[76] By superposing the ESP maps of molecular monomers, one can predict the relative stabilities of different configurations and gain insight into why certain configurations correspond to minima on the potential energy surface.

Based on this concept, we intuitively revealed the fundamental reasons behind the differences in the stability of various dimer configurations formed by H_2 and N_2 molecules.[76] In this study, high-precision quantum chemical calculations determined the relative stabilities of five key N_2 dimer configurations, following the order $Z \geq T > X > H > L$. The superposed ESP maps of the monomers for each configuration are shown in Fig. 15. As seen from the figure, the general trend is that the greater the overlap between the red and blue regions of the ESP maps, indicating stronger ESP complementarity, the more stable the corresponding configuration. For example, in the Z-configuration, which has the lowest electronic energy, there are two distinct regions where ESP signs are opposite, reflecting strong electrostatic attraction that significantly stabilizes this configuration. In contrast, the X-configuration exhibits both areas of ESP overlap with the same sign, indicating repulsion, and opposite signs, indicating attraction, resulting in a weak overall electrostatic stabilization. This explains why X is merely a metastable structure. Meanwhile, in the L-configuration, the ESP contour lines of both monomers overlap entirely with the same sign, leading to strong electrostatic repulsion. As a result, this configuration is highly unstable—not only does it have the highest energy among all configurations, but it is also not a true minimum on the potential energy surface. This study demonstrated that although the interaction between N_2 molecules is primarily driven by dispersion forces, as confirmed by energy decomposition analysis, electrostatic interactions still play a crucial role in determining the relative stabilities of different configurations. These effects can be effectively explained by simply visualizing the ESP complementarity of monomers.

Based on the similar ESP superposition analysis, Ref. [31] convincingly explained why the carbon atoms of two cyclo[18]carbon molecules in a π-π stacked dimer configuration are misaligned rather than exactly opposite each other. Additionally, Ref. [77] provided insight into the microscopic mechanism by which deep eutectic solvents, formed by 1-ethyl-3-methylimidazolium chloride and imidazole, efficiently capture SO_2.

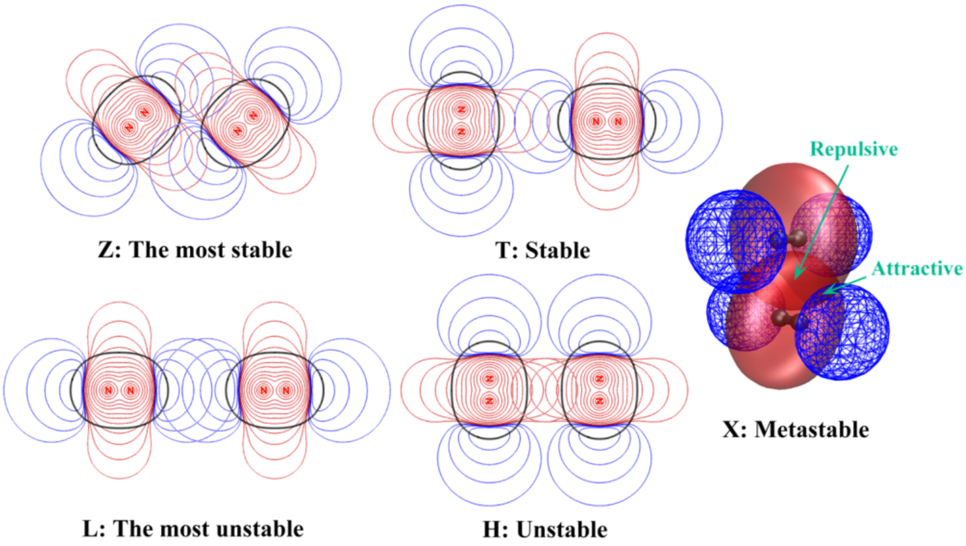

Figure 15 Superposition of ESP contour and isosurface maps of two N_2 molecule at different dimer configurations. Red and blue colors correspond to positive and negative ESP, respectively. Reprinted with permission from Ref. [76]. Copyright 2013 Springer Nature.

2.4.3 vdW potential analysis

In most cases, molecular interactions are primarily governed by electrostatic and vdW forces. When the electrostatic component is negligible, such as in interactions between nearly nonpolar molecules, the previously mentioned ESP analysis becomes less useful, whereas visualizing the vdW potential can be highly effective in explaining and predicting interactions. The definition of vdW potential and the concept of its visual analysis were introduced in our previous work, along with numerous application examples.[28]

In Ref. [78], we found that bicyclic oligoparaphenylenes (OPP) can stably adsorb cyclo[18]carbon, a molecule with extremely weak effective polarity.[31] The strong adsorption effect was intuitively explained through the vdW potential distribution of OPP. Fig. 16 presents the isosurface of the vdW potential of OPP at a specific negative value (-1.2 kcal·mol^{-1}), calculated using the carbon element as the probe. The region enclosed by the isosurface represents the area where the vdW attraction from OPP to a carbon atom is strongest. Notably, when cyclo[18]carbon is adsorbed within the OPP loop, most of its atoms fall precisely within this isosurface, visually demonstrating why the macrocyclic ring of OPP can stably accommodate cyclo[18]carbon. This example highlights how graphical analysis of vdW potential can be a powerful tool for understanding and predicting interactions and self-assembly processes involving nonpolar or weakly polar molecules. This approach has already been widely adopted in the study of vdW-dominated interactions in many other works.[79-84]

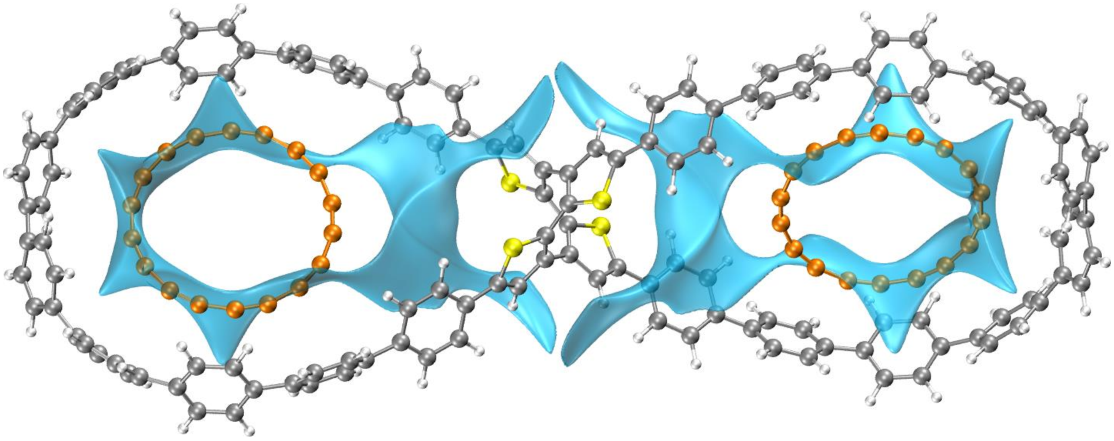

Figure 16. Isosurface map of vdW potential of OPP with isovalue of -1.2 kcal·mol^{-1}. Carbon is taken as the probe atom. The adsorbed cyclo[18]carbons are colored as orange and are placed at its actual position in the optimized complex. Adapted from from Ref. [78].

2.4.4 Energy decomposition analysis

Energy decomposition methods break down interaction energy into different physical components, providing deeper insights into the nature of molecular interactions. While the energy decomposition analysis based on molecular forcefields (EDA-FF), as implemented in the Multiwfn program, is not as precise as quantum chemistry-based methods such as SAPT[85] and sobEDA,[86] it offers a unique advantage: it can directly determine the contributions of different physical components to the interfragment interaction energy from individual atoms and atom pairs. This allows for the visualization of atomic contributions, helping researchers intuitively understand how each atom influences the noncovalent interaction of interest.

Fig. 17 illustrates the contributions of each atom to three key interaction components between two phenol molecules, represented by color mapping. The bluer (redder) the color, the more the atom strengthens (weakens) the intermolecular binding. The dispersion and exchange-repulsion components are evaluated using the GAFF forcefield,[87] while the electrostatic component is calculated based on CHELPG atomic charges.[50,88] The figure clearly highlights that the hydroxyl hydrogen of one phenol and the hydroxyl oxygen of the other contribute most significantly to intermolecular binding due to electrostatic attraction, which is the defining feature of a typical H-bond.[3] Additionally, other atoms in close intermolecular contact contribute notably to dispersion and exchange-repulsion interactions, indicating that vdW interactions also play a role in stabilizing the phenol dimer.

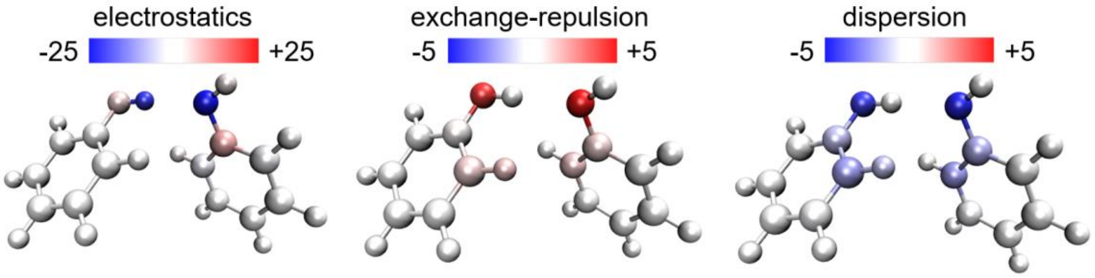

Figure 17. EDA-FF analysis result of the phenol dimer at the optimized configuration. Atoms are colored by their contributions to the three physical components of the intermolecular interaction energy. Reprinted with permission from Ref. [21,22]. Copyright 2024 AIP Publishing.

3. Visual Analysis of Covalent Interactions

3.1 ELF

In the inner shells of atoms, lone pair regions, and covalent bond regions, electron localization is significantly higher than in surrounding areas, making it more difficult for electrons in these regions to delocalize. The ELF, proposed by Becke and Edgecombe in 1990, is a three-dimensional real-space function specifically designed to show electron localization in different regions of a chemical system.[89] ELF is dimensionless, with a range of [0,1]. The closer the value is to 1, the stronger the electron localization at the corresponding position. ELF = 0.5 indicates electron localization similar to that of a non-interacting uniform electron gas. When plotting ELF, the focus is usually on regions where ELF > 0.5. In the valence region, if the ELF between two atoms is significantly greater than 0.5, it typically suggests a prominent covalent interaction between them, while regions with high ELF that do not appear between bonding atoms usually correspond to lone pairs or confined single electrons. This section will not provide a detailed introduction to the background theory of ELF or a comprehensive overview of its wide applications. Interested readers are referred to the relevant reviews.[90-93] The main aim of this section is to provide representative examples to help readers quickly understand how to use ELF to examine electronic structure, especially covalent interactions.

Fig. 18 presents ELF isosurfaces of a series of chemical systems. Fig. 18(a) shows ethane, ethylene, and acetylene. It can be seen that the ELF isosurfaces of the C-C single bond, double bond, and triple bond are all distributed in the bonding region, but their shapes differ significantly. The C-C single bond has an elliptical shape symmetrical around the bond axis, the double bond has a cone shape extending in the direction of π-electron distribution, and the triple bond has an oblate shape with a concave center, symmetrical around the bond axis. Since the shape of the ELF isosurface is highly sensitive to bond multiplicity, ELF can be used to visually detect bonding types. The multiple bonds between transition metals can also be displayed using ELF.[94,95] For example, Fig. 18(b) shows the Mo_2 molecule, which formally has a sextuple bond.[96] The ELF isosurface corresponding to this bond is a very large ring, as both the π- and δ-bonds between the two atoms are doubly degenerate.[96] Fig. 18(c) shows cyclopropane, where it can be seen that the center of the ELF isosurface corresponding to the C-C σ-bond is not exactly on the bond axis but deviates outward from the system. This demonstrates that ELF can faithfully reveal the offset of bonding electrons caused by ring strain. Fig. 18(d) shows a local region of C_{60} fullerene, where the ELF isosurfaces of the two types of C-C bonds in this system are both elongated perpendicularly to the bond axis, but the extent of elongation differs notably. This indicates that all C-C bonds in fullerene have a single π-interaction similar to the C-C bond in ethylene, but the strengths of the π-interactions in different bonds are clearly not the same. Fig. 18(e) presents the ELF map of $COCl_2$, which fully characterizes the C=O double bond, C-Cl single bond, two lone pairs on the O atom, and three lone pairs on the Cl atoms (the annular isosurface is a characteristic feature of this case). Fig. 18(f) corresponds to the Na crystal under very high pressure, where valence electrons can no longer freely delocalize over the system, and some localized electrons appear in the interstitial regions, which are also known as pseudoanions.[97] It can be seen that ELF can intuitively reveal the main distribution areas of these localized electrons.

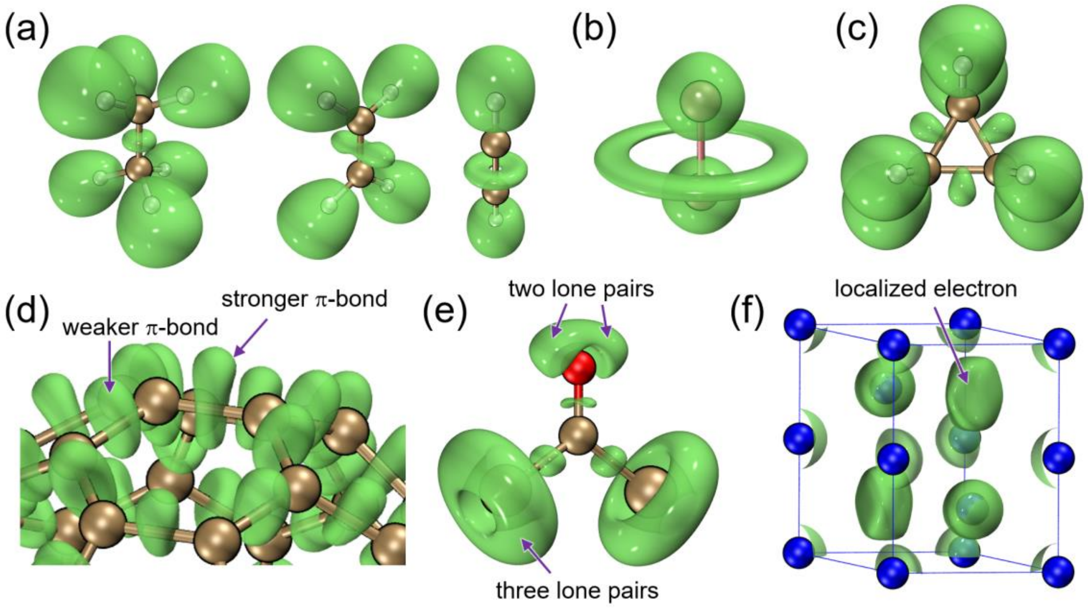

Figure 18. Isosurface maps of ELF of various systems. (a) ethane, ethene and acetylene, ELF=0.85 (b) Mo_2, ELF=0.58 (c) cyclopropane, ELF=0.85 (d) C_{60} fullerene, ELF=0.85 (e) $COCl_2$, ELF=0.85 (f) Na crystal of hP4 phase at 320 GPa, ELF=0.8.

ELF plane maps can often reveal more detailed information about bonding than ELF isosurface maps. Fig. 19 presents four typical examples. B_{11}^{-} is a planar system. Fig. 19(a) shows the color-filled ELF map on its molecular plane. As seen in the figure, this system not only contains the common covalent bonds between two atoms (two-center bonds, 2c-bonds), but also exhibits noticeable electron-sharing interactions between three atoms, namely the three-center bonds (3c-bonds). ELF effectively reveals both classical and non-classical covalent bonds, which is particularly important for studying the bonding in atomic cluster systems with complex electronic structures. Fig. 19(b) shows the ELF plane map of the contact area between the Au atom and the carbon atoms of the fullerene in the dumbbell-shaped $[C_{60}AuC_{60}]^+$ system reported by Goulart and coworkers.[98] The high localization areas indicated by the white arrows clearly demonstrate the existence of the covalent interaction between C_{60} and Au. Fig. 19(c) is a map from our study on the effect of external electric fields (EEF) on various properties of cyclo[18]carbon.[99] It can be seen that under the influence of a very strong EEF of 0.029 a.u., not only does the structure of cyclo[18]carbon change from a circle to an ellipse, but some of its electrons are almost detached from the system. Additionally, from the electron localization characteristics of the C-C bonds shown by ELF, it is evident that the strength of the C-C covalent bonds in this system alternates significantly. Fig. 19(d) shows potassium hydroxide. It is well known that there is an ionic bond between K and OH^-. From its ELF map, it can be seen that the electron localization in the bonding region is quite low. This is a typical feature of noncovalent interactions. Although ionic bonds cannot be directly displayed by ELF, they can be visualized using the methods introduced in Section 2, such as IRI, IGMH, and NCI.

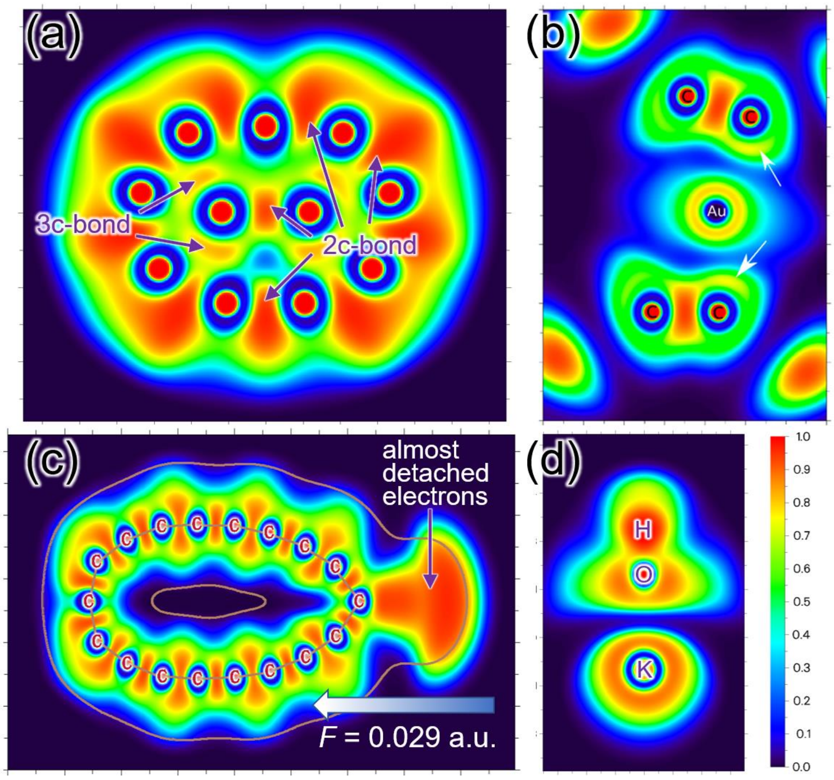

Figure 19. Color-filled plane maps of ELF of various systems. (a) B_{11}^- (b) Au@2C_{60}. Reprinted with permission from Ref. [98]. Copyright 2018 American Chemical Society. (c) cyclo[18]carbon under external electric field of strength of 0.029 a.u. Reprinted with permission from Ref. [99]. Copyright 2021 John Wiley and Sons. (d) Potassium hydroxide.

ELF can also be used to study changes in covalent bonding during reactions and *ab-initio* MD simulations, which is valuable for understanding reaction mechanisms and the evolution of covalent interactions over time. Due to space limitations, practical examples are not provided; interested readers are encouraged to refer to the relevant references.[91,100-103]

3.2 LOL

A function closely related to ELF is the localized orbital locator (LOL), proposed by Schmider and Becke in 2000.[104] Although its distribution characteristics are highly similar to those of ELF, and both are dimensionless functions with a range of [0,1], their definitions originate from different ideas. Localized molecular orbitals (LMOs) can be derived from unitary transformation of molecular orbitals, and their spatial distribution is highly localized. The LMOs representing valence electrons mainly appear in the regions where covalent bonds and lone pairs are located. The definition of the LOL function causes its value to be relatively large in the inner regions of LMOs and smaller in their boundary regions. According to our experience, in many cases, LOL provides better graphical representation than ELF. Specifically, the isosurface of LOL is easier to analyze visually, and it is often more effective at clearly displaying various covalent bonds and lone pairs in a single image. Therefore, when studying electronic structures such as covalent interactions and lone pair distributions, both LOL and ELF can be considered simultaneously. As an example, Fig. 20(a) shows the LOL isosurfaces of our recently theoretically predicted molecule, cyclo[18]nitrogen.[105] This map directly displays the lone pair on each nitrogen atom and also indicates that there are two types of N-N bonds in this system. The LOL isosurface of the N-N bond with pure α-bonding is cylindrically distributed around the bond axis, while the isosurface of the N-N double bond formed by α and π electrons is significantly elongated along the direction of the π-electron distribution. Fig. 20(b) shows the LOL map of Li_5^+, which rigorously demonstrates the presence of two four-center two-electron (4c-2e) interactions in this system, a common type of multi-center bond.

LOL-π and ELF-π refer to the LOL and ELF functions that are solely contributed by π-electrons, respectively.[42,106] They are highly useful for visually examining the bonding effects and delocalization of π-electrons and are widely applied in research on aromaticity.[106-109] Relatively speaking, the graphical representation of LOL-π is slightly more ideal than that of ELF-π, making LOL-π our preferred choice. Fig. 20(c) shows the LOL-π isosurface map of the experimentally synthesized twisted carbon nanobelt by Wu et al.[110] The isosurfaces cover a wide range of space, suggesting that the π-electrons can easily delocalize within the corresponding regions. However, at certain locations, indicated by the pink arrows, the very narrow isosurfaces imply that it is difficult for π-electrons to delocalize through these areas. sp^3 hybridized carbons do not have π-electrons, so their regions are completely uncovered by the LOL-π isosurfaces. This example highlights the convenience of using LOL-π to reveal the distribution and behavior of π-electrons.

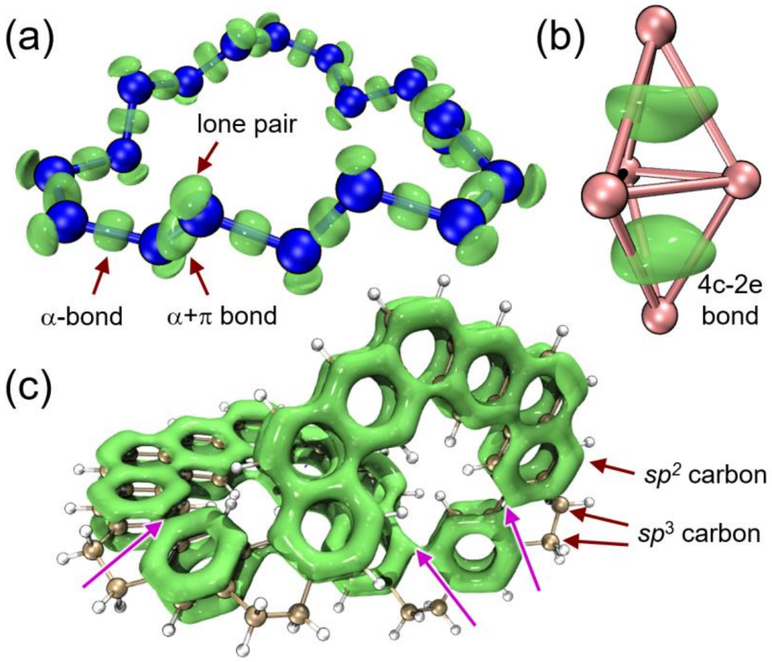

Figure 20. Isosurface maps of LOL of (a) cyclo[18]nitrogen and (b) Li_5^+, with LOL of 0.6 and 0.9, respectively. Isosurface map of LOL-π of a twisted carbon nanobelt with sp^2 and sp^3 carbons, isovalue of 0.4 is used.

3.3 Laplacian of electron density

The Laplacian of electron density, $\nabla^2\rho$, is a function extensively employed in QTAIM theory.[26] Notable positive and negative values of this function indicate that electron density is locally concentrated and depleted at the corresponding positions, respectively.[26,57,111,112] In regions where covalent bonds are formed between elements in the first few periods, the value of this function is usually negative, so one can plot $\nabla^2\rho$ isosurfaces or plane maps to visually identify the atoms that are covalently bonded. The usefulness of $\nabla^2\rho$ in revealing covalent interactions is similar to that of ELF and LOL. However, since the $\nabla^2\rho$ map often involves a very wide range of values, its graphical representation of covalent interaction areas is often not as ideal as ELF and LOL; additionally, it cannot effectively reveal covalent bonds between heavy atoms, such as the covalent bond in I_2 molecules. Therefore, $\nabla^2\rho$ is less commonly used today for visually studying covalent interactions. Interested readers are encouraged to refer to Bader's article, which specifically compares $\nabla^2\rho$ and ELF,[113] and more examples of $\nabla^2\rho$ analysis can be found in Refs. [26,57,112,114].

3.4 Deformation density

The formation of a covalent bond is generally accompanied by a significant increase in electron density in the bonding region. Deformation density (ρ^{def}) is defined as the difference between the actual electron density and ρ^{pro},[21,114,115] and it reflects all changes in electron density distribution caused by atomic interactions. Clearly, if the values between two or more atoms are markedly positive in the ρ^{def} map, it indicates the formation of covalent interactions between them. Plotting a ρ^{def} map is an ideal method for studying covalent interactions, as its physical meaning is clear, the map is easy to visually analyze, and it is applicable to the bonding between any elements. However, ρ^{def} is currently less popular than ELF and LOL, mainly because only a few programs, such as Multiwfn, can conveniently plot it. Fig. 21 presents an example of the ρ^{def} map, where solid red lines and blue dashed lines correspond to regions with increases and decreases in electron density, respectively, due to the formation of this system from isolated atoms. It is clearly evident that the Re-Re and Re-Cl interactions must be attributed to covalent bonds, as the ρ^{def} in the interaction areas shows a prominently positive value.

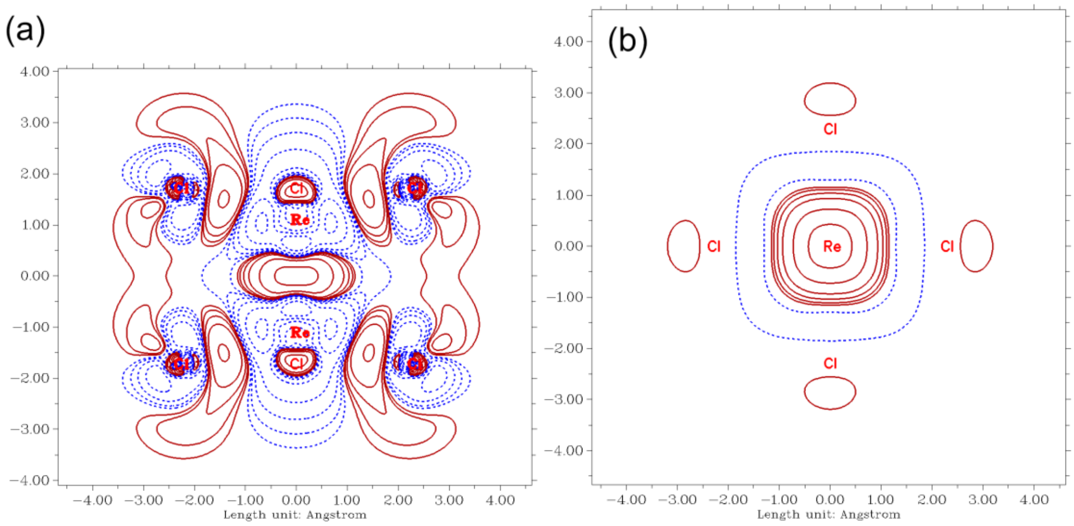

Figure 21. Contour line map of deformation density of $[Re_2Cl_8]^{2-}$ anion, two views are given. Solid red lines and blue dashed lines correspond to positive and negative regions, respectively.

3.5 Valence electron density

The electron distribution characteristics in various chemical systems are highly consistent; that is, the overall distribution of electron density decreases exponentially from each nucleus to the surrounding areas. As a result, directly plotting the total electron density typically does not provide useful information for studying chemical bonds. The valence electron density (ρ^{val}) refers to the electron density obtained by removing the contribution of inner electrons from the total electron density. We have found that the ρ^{val} map is very useful for studying covalent bonding in many cases.[114] Not only is its visualization as intuitive as that of ELF, LOL, and ρ^{def}, but its calculation is also straightforward (only the inner core orbitals need to be excluded when calculating the electron density) and less time-consuming (as there is no need to compute derivatives of the electron density or wavefunction). However, the value of ρ^{val} in bonding analysis has long been underestimated.

Here, only one representative analysis instance from Ref. [114] is provided, and more illustrations of ρ^{val} can also be found in the same work. Fig. 22 shows the energy variation of the Diels-Alder reaction between 1,3-butadiene and ethene, with ρ^{val} isosurface maps attached for some key points along the intrinsic reaction path. First, it can be observed that the ρ^{val} isosurfaces intuitively show the distribution of electrons involved in bonding. Based on the size of the isosurfaces in the bonding areas, the relative strength of the C-C bonds can be easily inferred. For example, in structure (a), the ρ^{val} between atoms of the typical double bond (C5-C6) and the approximate double bonds (C1-C2 and C3-C4) is much higher than that between C2-C3, which is close to a single bond.[111] As the reaction progresses, it is clearly seen from the figure that the ρ^{val} on the C1-C2 and C5-C6 bonds gradually decreases, while the ρ^{val} on the C2-C3 bond gradually increases. At the transition state structure, the isosurfaces of all C-C bonds are almost the same, indicating that the strengths of these bonds are nearly indistinguishable. In the product structure (d), the ρ^{val} distribution on the C2-C3 bond is roughly equivalent to that of the C5-C6 bond in the reactant structure, reflecting that the C2-C3 bond has finally become a double bond. Additionally, in the final structure, the ρ^{val} on the C1-C2 bond is slightly higher than that on the C1-C5 and C4-C6 bonds, indicating that the C1-C2 bond is slightly stronger, which can also be confirmed by calculating the Laplacian bond order.[111] This example demonstrates that the smooth variation in bonding characteristics during an organic reaction can be successfully revealed by tracing the change in the ρ^{val} map, highlighting the significant value of visual analysis of ρ^{val}.

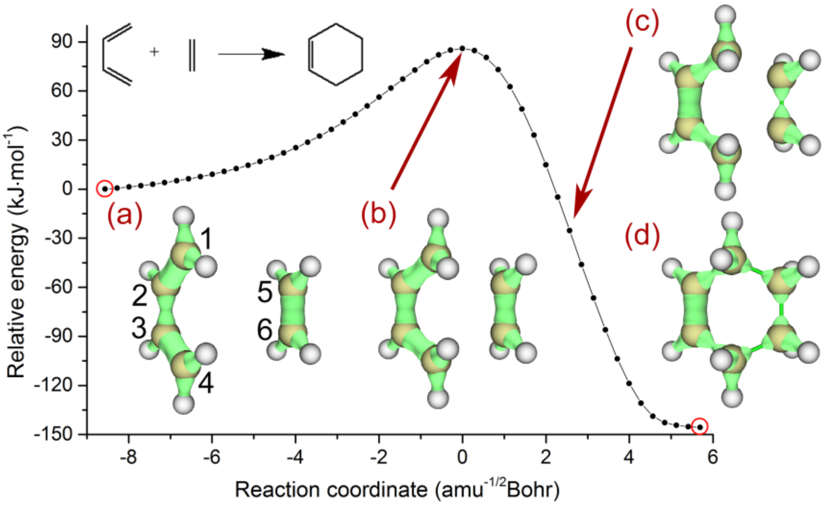

Figure 22. Energy variation along intrinsic reaction path (IRC) of Diels-Alder reaction between 1,3-butadiene and ethene. Isosurfaces of valence electron density of reactant (a), transition state (b), a featured IRC point (c) and product (d) are plotted as insets. Isovalues of all graphs are set to 0.25 a.u. Indices of carbon atoms are labelled in (a). Reprinted with permission from Ref. [114]. Copyright 2018 Editorial Office of Acta Physico-Chimica Sinica.

There are also other real-space functions may be used for visual study of covalent interactions, they are not introduced here due to the length of the article. These methods include: bond order density (BOD),[116] strong covalent interaction (SCI),[94,95] phase-space-defined Fisher information density (PS-FID),[117] region of slow electrons (RoSE),[118] electron localizability indicator (ELI),[119] single exponential decay detector (SEDD),[120] electron delocalization range function (EDR),[121] $\nabla^2\delta_{\text{He}}$.[122]

4. Computer Codes for Visual Analysis of Interactions

In the field of computational chemistry, many computer programs can perform the analyses described above, such as IGMplot for IGM and IGM(GBP) analyses,[123] NCIplot for NCI and NCI^{pro} analyses,[124] and CrystalExplorer for HSA.[68] The widely used ELF can be calculated by various codes, including Topmod[125] and CP2K.[30] However, the Multiwfn wavefunction analysis program,[21,22] which we have been developing since 2009, is the only program capable of performing all the aforementioned analysis methods. Except for Fig. 14(a), the data for all examples in this review were generated by the present author or the corresponding reference authors using the Multiwfn program. Our purpose in developing Multiwfn is to provide chemists with a comprehensive, easy-to-use, highly efficient, and open-source analysis tool. It has now become one of the most popular post-processing analysis programs in the computational chemistry field. The executable file and source code of Multiwfn can be freely downloaded from its official homepage: http://sobereva.com/multiwfn. Analysis of real-space functions is one of key strengths of Multiwfn, with more than one hundred real-space functions implemented in this code. The analysis of real-space functions in Multiwfn not only supports isolated systems but also ideally supports periodic systems, making visualization analysis applicable not only to molecules and clusters but also to solids and surface systems. Multiwfn features a plotting function capable of displaying isosurface, plane, and curve maps for the calculated real-space functions. To obtain the color-filled isosurface maps involved in analyses such as IRI, IGMH, and amIGM, Multiwfn can export the calculated grid data to .cub files. One can then easily generate the corresponding maps using the freely available VMD software with the plotting scripts included in the Multiwfn package.

Using Multiwfn to perform analyses such as IRI, IGMH, ESP, and ELF requires the user to supply a file containing wavefunction information in formats such as .wfn, .mwfn,[126] .molden, and .fch. Most mainstream quantum chemistry programs, such as Gaussian,[127] ORCA,[128] GAMESS-US,[129] and the first-principles program

CP2K, can export wavefunction data in at least one of these formats. For mIGM, HSA, vdW potential, and some other analyses, the user only needs to supply Multiwfn with a file containing the element and coordinate information of the atoms in the system. Common formats, such as .xyz, .pdb, .mol2, and .cif, can be used for this purpose. For aNCI and amIGM, which involve time-averaging, a multi-frame .xyz file containing the MD trajectory is required, which can be converted using VMD from the trajectory file produced by MD programs such as GROMACS.[130]

For more information about Multiwfn, see the recent introductory article.[21] Multiwfn has a highly detailed manual of more than 1,100 pages and includes a vast number of tutorials, through which chemists can easily learn how to use Multiwfn to perform analyses and readily apply them to their own research.

5. Conclusions

The visual analysis of interactions in chemical systems is a rapidly growing research field and is becoming increasingly popular. In recent years, new analysis methods of this type have been continuously proposed. This article comprehensively introduces both classic and recently developed methods for the visual analysis of covalent and noncovalent interactions and briefly mentions the Multiwfn program, which can implement these analyses.

From the examples in this article, readers should find that these analysis methods are highly useful for chemists to quickly understand the characteristics and strengths of interactions of interest in an intuitive manner. As a result, computational chemists no longer need to constantly deal with large amounts of complex and abstract numerical data generated by theoretical calculations. The vivid images produced by these methods are also well-suited for inclusion in textbooks and undergraduate chemistry education, helping students gain a clearer understanding of interactions in various systems and fostering their interest in theoretical chemistry.

There remains significant room for further development of visualization-based analysis methods. Future advancements may focus on designing methods with improved graphical effects, richer representations of interaction-related information, and more powerful techniques that closely link intuitive visualizations with accurate interaction energies and their physical components.

Acknowledgments

This research was not funded.

Conflicts of interest

The authors declare no conflict of interest.

References

[1] M. Waller, S. Grimme, Weak Intermolecular Interactions: A Supermolecular Approach. In Handbook of Computational Chemistry, J. Leszczynski, A. Kaczmarek-Kedziera, T. Puzyn, M. G. Papadopoulos, H. Reis, M. K. Shukla, Eds., Springer International Publishing: Cham, **2017**, p. 593.

[2] L. Rummel, P. R. Schreiner, *Angew. Chem. Int. Ed.* **2024**, *63*, e202316364

[3] S. Emamian, T. Lu, H. Kruse, H. Emamian, *J. Comput. Chem.* **2019**, *40*, 2868

[4] S. J. Grabowski, *Chem. Rev.* **2011**, *111*, 2597

[5] T. Steiner, *Angew. Chem. Int. Ed.* **2002**, *41*, 48

[6] T. Clark, M. Hennemann, J. Murray, P. Politzer, *J. Mol. Model.* **2007**, *13*, 291

[7] P. Politzer, P. Lane, M. Concha, Y. Ma, J. Murray, *J. Mol. Model.* **2007**, *13*, 305

[8] F. Zhou, Y. Liu, Z. Wang, T. Lu, Q. Yang, Y. Liu, B. Zheng, *Phys. Chem. Chem. Phys.* **2019**, *21*, 15310

[9] D. J. Pascoe, K. B. Ling, S. L. Cockroft, *J. Am. Chem. Soc.* **2017**, *139*, 15160

[10] V. Oliveira, D. Cremer, E. Kraka, *J. Phys. Chem. A* **2017**, *121*, 6845

[11] V. Oliveira, E. Kraka, *J. Phys. Chem. A* **2017**, *121*, 9544

[12] Y. Jiao, Y. Liu, W. Zhao, Z. Wang, X. Ding, H. Liu, T. Lu, *Int. J. Quantum Chem.* **2017**, *117*, e25443

[13] J. S. Murray, P. Lane, P. Politzer, *J. Mol. Model.* **2009**, *15*, 723

[14] D. Mani, E. Arunan, *Phys. Chem. Chem. Phys.* **2013**, *15*, 14377

[15] P. Lipkowski, S. J. Grabowski, T. L. Robinson, J. Leszczynski, *J. Phys. Chem. A* **2004**, *108*, 10865

[16] Z. Zhang, T. Lu, L. Ding, G. Wang, Z. Wang, B. Zheng, Y. Liu, X. L. Ding, *Mol. Phys.* **2020**, *118*, e1784478

[17] B. Zheng, Y. Liu, Z. Wang, F. Zhou, Y. Liu, X. Ding, T. Lu, *Mol. Phys.* **2019**, *117*, 2443

[18] S. Grimme, *Angew. Chem. Int. Ed.* **2008**, *47*, 3430

[19] Z. Liu, T. Lu, *Chem.-Eur. J.* **2024**, *30*, e202402227

[20] N. Elghobashi, L. González, *J. Chem. Phys.* **2006**, *124*

[21] T. Lu, *J. Chem. Phys.* **2024**, *161*

[22] T. Lu, F. Chen, *J. Comput. Chem.* **2012**, *33*, 580

[23] E. R. Johnson, S. Keinan, P. Mori-Sánchez, J. Contreras-García, A. J. Cohen, W. Yang, *J. Am. Chem. Soc.* **2010**, *132*, 6498

[24] T. Lu, Q. Chen, Visualization Analysis of Weak Interactions in Chemical Systems. In Comprehensive Computational Chemistry 2, Elsevier, **2023**, p. 240.

[25] J. P. Perdew, W. Yue, *Phys. Rev. B* **1986**, *33*, 8800

[26] F. W. Bader, Atoms in Molecules: A Quantum Theory, Oxford University Press: New York, 1994.

[27] E. Solel, M. Ruth, P. R. Schreiner, *J. Am. Chem. Soc.* **2021**, *143*, 20837

[28] T. Lu, Q. Chen, *J. Mol. Model.* **2020**, *26*, 315

[29] I. González-Veloso, J. A. Carrazana-García, D. Josa, J. Rodríguez-Otero, E. M. Cabaleiro-Lago, *Comput. Theor. Chem.* **2015**, *1053*, 123

[30] T. D. Kühne, M. Iannuzzi, M. Del Ben, V. V. Rybkin, P. Seewald, F. Stein, T. Laino, R. Z. Khaliullin, O. Schütt, F. Schiffmann, D. Golze, J. Wilhelm, S. Chulkov, M. H. Bani-Hashemian, V. Weber, U. Borštnik, M. Taillefumier, A. S. Jakobovits, A. Lazzaro, H. Pabst, T. Müller, R. Schade, M. Guidon, S. Andermatt, N. Holmberg, G. K. Schenter, A. Hehn, A. Bussy, F. Belleflamme, G. Tabacchi, A. Glöß, M. Lass, I. Bethune, C. J. Mundy, C. Plessl, M. Watkins, J. VandeVondele, M. Krack, J. Hutter, *J. Chem. Phys.* **2020**, *152*, 194103

[31] Z. Liu, T. Lu, Q. Chen, *Carbon* **2021**, *171*, 514

[32] T. Lu, S. Manzetti, *Struct. Chem.* **2014**, *25*, 1521

[33] R. Laplaza, F. Peccati, R. A. Boto, C. Quan, A. Carbone, J.-P. Piquemal, Y. Maday, J. Contreras-García, *WIREs Comput. Mol. Sci.* **2021**, *11*, e1497

[34] R. A. Boto, F. Peccati, R. Laplaza, C. Quan, A. Carbone, J.-P. Piquemal, Y. Maday, J. Contreras-García, *J. Chem. Theory Comput.* **2020**, *16*, 4150

[35] J. Contreras-García, W. Yang, E. R. Johnson, *J. Phys. Chem. A* **2011**, *115*, 12983

[36] G. Saleh, C. Gatti, L. Lo Presti, *Comput. Theor. Chem.* **2015**, *1053*, 53

[37] J. Contreras-García, R. A. Boto, F. Izquierdo-Ruiz, I. Reva, T. Woller, M. Alonso, *Theor. Chem. Acc.* **2016**, *135*, 242

[38] D. Morales-Pumarino, J. E. Barquera-Lozada, *Int. J. Quantum Chem.* **2023**, *123*, e27051

[39] N. Gillet, R. Chaudret, J. Contreras-García, W. Yang, B. Silvi, J.-P. Piquemal, *J. Chem. Theory Comput.* **2012**, *8*, 3993

[40] P. de Silva, C. Corminboeuf, *J. Chem. Theory Comput.* **2014**, *10*, 3745

[41] T. Lu, Q. Chen, *Chemistry-Methods* **2021**, *1*, 231

[42] T. Lu, Q. Chen, *Theor. Chem. Acc.* **2020**, *139*, 25

[43] X. Wang, Z. Liu, X. Yan, T. Lu, W. Zheng, W. Xiong, *Chem.-Eur. J.* **2022**, *28*, e202103815

[44] Z. Liu, T. Lu, Q. Chen, *Carbon* **2020**, *165*, 468

[45] W. Gao, L. Cai, F. Kang, L. Shang, M. Zhao, C. Zhang, W. Xu, *J. Am. Chem. Soc.* **2023**, *145*, 6203

[46] C. Lefebvre, G. Rubez, H. Khartabil, J.-C. Boisson, J. Contreras-García, E. Hénon, *Phys. Chem. Chem. Phys.* **2017**, *19*, 17928

[47] T. Lu, Q. Chen, *J. Comput. Chem.* **2022**, *43*, 539

[48] T. Lu, Q. Chen, *ChemRxiv* **2022**. DOI: 10.26434/chemrxiv-2022-g1m34

[49] F. L. Hirshfeld, *Theor. Chem. Acc.* **1977**, *44*, 129

[50] T. Lu, Q. Chen, Partial Charges. In Exploring Chemical Concepts Through Theory and Computation, S. Liu, Ed., WILEY-VCH GmbH: Weinheim, **2024**, p. 161.

[51] C. Lefebvre, H. Khartabil, J.-C. Boisson, J. Contreras-García, J.-P. Piquemal, E. Hénon, *ChemPhysChem* **2018**, *19*, 724

[52] T. Lu, *ChemRxiv* **2025**. DOI: 10.26434/chemrxiv-2025-zts13

[53] W.-F. Zheng, J. Chen, X. Qi, Z. Huang, *Nat. Chem.* **2023**, *15*, 1672

[54] R. Gao, Z. Liu, Z. Liu, T. Liang, J. Su, L. Gan, *Angew. Chem. Int. Ed.* **2023**, *62*, e202300151

[55] M. Ponce-Vargas, C. Lefebvre, J.-C. Boisson, E. Hénon, *J. Chem. Inf. Model.* **2020**, *60*, 268

[56] J. Klein, H. Khartabil, J.-C. Boisson, J. Contreras-García, J.-P. Piquemal, E. Hénon, *J. Phys. Chem. A* **2020**, *124*, 1850

[57] C. F. Matta, R. J. Boyd, Eds. The Quantum Theory of Atoms in Molecules - From Solid State to DNA and Drug Design; WILEY-VCH Verlag GmbH & Co. KGaA: Weinheim, 2007.

[58] B. Niepötter, R. Herbst-Irmer, D. Kratzert, P. P. Samuel, K. C. Mondal, H. W. Roesky, P. Jerabek, G. Frenking, D. Stalke, *Angew. Chem. Int. Ed.* **2014**, *53*, 2766

[59] R. Bianchi, G. Gervasio, D. Marabello, *Inorg. Chem.* **2000**, *39*, 2360

[60] D. Cremer, E. Kraka, *Angew. Chem. Int. Ed. Engl.* **1984**, *23*, 627

[61] J. R. Lane, J. Contreras-García, J.-P. Piquemal, B. J. Miller, H. G. Kjaergaard, *J. Chem. Theory Comput.* **2013**, *9*, 3263

[62] A. R. Leach, Molecular modelling Principles and applications, Pearson Education: Essex, 2001.

[63] P. Wu, R. Chaudret, X. Hu, W. Yang, *J. Chem. Theory Comput.* **2013**, *9*, 2226

[64] J. Gao, G. Zhang, Y.-W. Zhang, *Sci. Rep.* **2016**, *6*, 29107

[65] J. Zhang, L. Zhang, Y. Xu, S. Jiang, Y. Shao, *PLoS One* **2018**, *13*, e0196651

[66] M.-R. Li, N. Zhang, F.-S. Zhang, *Chin. Phys. B.* **2018**, *27*, 083103

[67] M. A. Spackman, P. G. Byrom, *Chem. Phys. Lett.* **1997**, *267*, 215

[68] M. A. Spackman, D. Jayatilaka, *CrystEngComm* **2009**, *11*, 19

[69] J. J. McKinnon, M. A. Spackman, A. S. Mitchell, *Acta Crystallographica Section B* **2004**, *60*, 627

[70] S. Irii, T. Ogaki, H. Miyashita, K. Nobori, Y. Ozawa, M. Abe, H. Sato, E. Ohta, Y. Matsui, H. Ikeda, *Tetrahedron Lett.* **2022**, *101*, 153913

[71] J. S. Murray, P. Politzer, *WIREs: Comp. Mol. Sci.* **2011**, *1*, 153

[72] P. Politzer, J. S. Murray, The Electrostatic Potential as a Guide to Molecular Interactive Behavior. In Chemical Reactivity Theory: A Density Functional View, P. K. Chattaraj, Ed., CRC Press: Boca Raton, **2009**.

[73] P. Politzer, J. S. Murray, *Theor. Chem. Acc.* **2002**, *108*, 134

[74] J. S. Murray, P. Politzer, In Encyclopedia of Computational Chemistry; P. v. R. Schleyer, Ed.; John Wiley & Sons: West Sussex, 1998, p 912.

[75] P. Politzer, J. S. Murray, Molecular Electrostatic Potentials and Chemical Reactivity. In Reviews in Computational Chemistry 2, K. B. Lipkowitz, D. B. Boyd, Eds., John Wiley & Sons, Inc.: New York, **1991**, p. 273.

[76] T. Lu, F. Chen, *J. Mol. Model.* **2013**, *19*, 5387

[77] Z.-L. Li, L.-S. Zhou, Y.-H. Wei, H.-L. Peng, K. Huang, *Ind. Eng. Chem. Res.* **2020**, *59*, 13696

[78] Z. Liu, X. Wang, T. Lu, J. Wang, X. Yan, Y. Wu, J. Xu, *Phys. Chem. Chem. Phys.* **2023**, *25*, 16707

[79] J. Yi, L. Pei, D. Lu, S. Sun, W. Cheng, G. Sun, J. Zhao, J. Wang, *Cellulose* **2025**, *32*, 2041

[80] C. Gui, D. Xiang, M. Feng, C. Guo, S. Fourmentin, *Sep. Purif. Technol.* **2025**, *360*, 131121

[81] Y.-q. Yang, Q. Gao, S.-q. Yue, X. Peng, N. Wang, J.-l. Xin, M. Yu, J.-j. Rao, Y.-l. Xue, *Food Chem.* **2025**, *463*, 141435

[82] W. Zhang, F. Luo, Z. Gao, H. Chi, J. Wang, F. Yu, Y.-P. He, *Colloids and Interfaces* **2024**, *8*

[83] H. Jia, H. Jia, Q. Wang, X. Wei, H. Yan, Y. Wang, Q. Wang, K. Lv, P. Huang, *J. Mol. Liq.* **2024**, *408*, 125378

[84] B. Li, H. Xu, Y. Dang, K. N. Houk, *J. Am. Chem. Soc.* **2022**, *144*, 1971

[85] K. Szalewicz, *WIREs: Comp. Mol. Sci.* **2012**, *2*, 254

[86] T. Lu, Q. Chen, *J. Phys. Chem. A* **2023**, *127*, 7023

[87] J. Wang, R. M. Wolf, J. W. Caldwell, P. A. Kollman, D. A. Case, *J. Comput. Chem.* **2004**, *25*, 1157

[88] C. M. Breneman, K. B. Wiberg, *J. Comput. Chem.* **1990**, *11*, 361

[89] A. D. Becke, K. E. Edgecombe, *J. Chem. Phys.* **1990**, *92*, 5397

[90] T. Lu, F. Chen, *Acta Phys. -Chim. Sin.* **2011**, *27*, 2786

[91] P. Fuentealba, E. Chamorro, J. C. Santos, Understanding and using the electron localization function. In Theoretical Aspects of Chemical Reactivity, A. Toro-Labbé, Ed., Elsevier B.V.: Amsterdam, **2007**, p. 57.

[92] A. Savin, R. Nesper, S. Wengert, T. F. Fässler, *Angew. Chem. Int. Ed. Engl.* **1997**, *36*, 1808

[93] B. Silvi, The Relevance of the ELF Topological Approach to the Lewis, Kossel, and Langmuir Bond Model. In The Chemical Bond II: 100 Years Old and Getting Stronger, D. M. P. Mingos, Ed., Springer International Publishing: Cham, **2016**, p. 213.

[94] Y. Huang, L. Liu, C. Rong, T. Lu, P. W. Ayers, S. Liu, *J. Mol. Model.* **2018**, *24*, 213

[95] S. Liu, C. Rong, T. Lu, H. Hu, *J. Phys. Chem. A* **2018**, *122*, 3087

[96] B. O. Roos, A. C. Borin, L. Gagliardi, *Angew. Chem.* **2007**, *119*, 1491

[97] M. Marqués, M. Santoro, C. L. Guillaume, F. A. Gorelli, J. Contreras-García, R. T. Howie, A. F. Goncharov, E. Gregoryanz, *Phys. Rev. B* **2011**, *83*, 184106

[98] M. Goulart, M. Kuhn, P. Martini, L. Chen, F. Hagelberg, A. Kaiser, P. Scheier, A. M. Ellis, *J. Phys. Chem. Lett.* **2018**, *9*, 2703

[99] T. Lu, Q. Chen, *ChemPhysChem* **2021**, *22*, 386

[100] S. Emamian, T. Lu, F. Moeinpour, *RSC Adv.* **2015**, *5*, 62248

[101] T. Burnus, M. A. L. Marques, E. K. U. Gross, *Phys. Rev. A* **2005**, *71*, 010501

[102] V. Polo, J. Andres, S. Berski, L. R. Domingo, B. Silvi, *J. Phys. Chem. A* **2008**, *112*, 7128

[103] E. Chamorro, *J. Chem. Phys.* **2001**, *114*, 23

[104] H. L. Schmider, A. D. Becke, *J. Mol. Struct. (THEOCHEM)* **2000**, *527*, 51

[105] T. Lu, *ChemPhysChem* **2024**, *25*, e202400377

[106] J. C. Santos, W. Tiznado, R. Contreras, P. Fuentealba, *J. Chem. Phys.* **2004**, *120*, 1670

[107] Y. Wu, Z. Liu, T. Lu, M. Orozco-Ic, J. Xu, X. Yan, J. Wang, X. Wang, *Inorg. Chem.* **2023**, *62*, 19986

[108] X. Wang, Z. Liu, J. Wang, T. Lu, W. Xiong, X. Yan, M. Zhao, M. Orozco-Ic, *Chem.-Eur. J.* **2023**, *29*, e202300348

[109] Z. Liu, T. Lu, S. Hua, Y. Yu, *J. Phys. Chem. C* **2019**, *123*, 18593

[110] W. Fan, T. Matsuno, Y. Han, X. Wang, Q. Zhou, H. Isobe, J. Wu, *J. Am. Chem. Soc.* **2021**, *143*, 15924

[111]T. Lu, F. Chen, *J. Phys. Chem. A* **2013**, *117*, 3100

[112] Z. Shi, R. J. Boyd, *J. Phys. Chem.* **1991**, *95*, 4698

[113] R. F. W. Bader, S. Johnson, T. H. Tang, P. L. A. Popelier, *J. Phys. Chem.* **1996**, *100*, 15398

[114] T. Lu, Q. Chen, *Acta Phys. -Chim. Sin.* **2018**, *34*, 503

[115] C. F. Guerra, J.-W. Handgraaf, E. J. Baerends, F. M. Bickelhaupt, *J. Comput. Chem.* **2004**, *25*, 189

[116] J. L. Casals-Sainz, A. Fernández-Alarcón, E. Francisco, A. Costales, Á. Martín Pendás, *J. Phys. Chem. A* **2020**, *124*, 339

[117] A. A. Astakhov, V. G. Tsirelson, *Chem. Phys.* **2014**, *435*, 49

[118] H. Jacobsen, *Chem. Phys. Lett.* **2013**, *582*, 144

[119] V. Bezugly, P. Wielgus, M. Kohout, F. R. Wagner, *J. Comput. Chem.* **2010**, *31*, 1504

[120] P. de Silva, J. Korchowiec, T. A. Wesolowski, *ChemPhysChem* **2012**, *13*, 3462

[121] B. G. Janesko, G. Scalmani, M. J. Frisch, *J. Chem. Phys.* **2014**, *141*

[122] E. Y. Tupikina, A. A. Efimova, G. S. Denisov, P. M. Tolstoy, *J. Comput. Chem.* **2018**, *39*, 2459

[123] C. Lefebvre, J. Klein, H. Khartabil, J. C. Boisson, E. Hénon, *J. Comput. Chem.* **2023**, *44*, 1750

[124] J. Contreras-García, E. R. Johnson, S. Keinan, R. Chaudret, J.-P. Piquemal, D. N. Beratan, W. Yang, *J. Chem. Theory Comput.* **2011**, *7*, 625

[125] S. Noury, X. Krokidis, F. Fuster, B. Silvi, *Comput. Chem.* **1999**, *23*, 597

[126] T. Lu, Q. Chen, *ChemRxiv* **2020**. DOI: 10.26434/chemrxiv-2021-lt04f-v6

[127] M. J. Frisch, G. W. Trucks, H. B. Schlegel, G. E. Scuseria, M. A. Robb, J. R. Cheeseman, G. Scalmani, V. Barone, G. A. Petersson, H. Nakatsuji, X. Li, M. Caricato, A. V. Marenich, J. Bloino, B. G. Janesko, R. Gomperts, B. Mennucci, H. P. Hratchian, J. V. Ortiz, A. F. Izmaylov, J. L. Sonnenberg, Williams, F. Ding, F. Lipparini, F. Egidi, J. Goings, B. Peng, A. Petrone, T. Henderson, D. Ranasinghe, V. G. Zakrzewski, J. Gao, N. Rega, G. Zheng, W. Liang, M. Hada, M. Ehara, K. Toyota, R. Fukuda, J. Hasegawa, M. Ishida, T. Nakajima, Y. Honda, O. Kitao, H. Nakai, T. Vreven, K. Throssell, J. A. Montgomery Jr., J. E. Peralta, F. Ogliaro, M. J. Bearpark, J. J. Heyd, E. N. Brothers, K. N. Kudin, V. N. Staroverov, T. A. Keith, R. Kobayashi, J. Normand, K. Raghavachari, A. P. Rendell, J. C. Burant, S. S. Iyengar, J. Tomasi, M. Cossi, J. M. Millam, M. Klene, C. Adamo, R. Cammi, J. W. Ochterski, R. L. Martin, K. Morokuma, O. Farkas, J. B. Foresman, D. J. Fox, Gaussian 16 A.03. Wallingford, CT, **2016**.

[128] F. Neese, F. Wennmohs, U. Becker, C. Riplinger, *J. Chem. Phys.* **2020**, *152*, 224108

[129] G. M. J. Barca, C. Bertoni, L. Carrington, D. Datta, N. De Silva, J. E. Deustua, D. G. Fedorov, J. R. Gour, A. O. Gunina, E. Guidez, T. Harville, S. Irle, J. Ivanic, K. Kowalski, S. S. Leang, H. Li, W. Li, J. J. Lutz, I. Magoulas, J. Mato, V. Mironov, H. Nakata, B. Q. Pham, P. Piecuch, D. Poole, S. R. Pruitt, A. P. Rendell, L. B. Roskop, K. Ruedenberg, T. Sattasathuchana, M. W. Schmidt, J. Shen, L. Slipchenko, M. Sosonkina, V. Sundriyal, A. Tiwari, J. L. Galvez Vallejo, B. Westheimer, M. Włoch, P. Xu, F. Zahariev, M. S. Gordon, *J. Chem. Phys.* **2020**, *152*

[130] M. J. Abraham, T. Murtola, R. Schulz, S. Páll, J. C. Smith, B. Hess, E. Lindahl, *SoftwareX* **2015**, *1*, 19